Title: The actomyosin cortex controls t-tubule remodeling in muscle

Authors: Ana Raquel Pereira[†1,2], Ana da Rosa Soares[†1,2], Silvia Di Francescantonio[1,2], Tianyang Liu[3], Filomena A. Carvalho[1,2], Josie Liane Ferreira[3,4], Graciano Leal[1,2], Inês Faleiro[1,2], Naoko Kogata[5], Nuno C. Santos[1,2], Michael Way[5,6], Carolyn A. Moores[3], Edgar R. Gomes*[1,2]

Affiliations:

[1] GIMM - Gulbenkian Institute for Molecular Medicine, Avenida Prof. Egas Moniz, 1649-028 Lisboa, Portugal

[2] Faculdade de Medicina, Universidade de Lisboa, Av. Prof. Egas Moniz, 1649-028 Lisboa, Portugal.

[3] Institute of Structural and Molecular Biology, Birkbeck College, London, WC1E 7HX, UK

[4] Institute of Structural and Molecular Biology, Division of Biosciences, University College London, London WC1E 6BT, UK

[5] Cellular signalling and cytoskeletal function laboratory, The Francis Crick Institute, 1 Midland Road, London, NW1 1AT, UK

[6] Department of Infectious Disease, Imperial College, London SW7 2AZ, UK

* corresponding author: edgar.gomes@gimm.pt

† these authors contributed equally to this work

Abstract: Muscle cells form a network of plasma membrane invaginations called t-tubules that control calcium release from the endoplasmic reticulum at the triads during muscle contraction. Although the importance of t-tubules for muscle physiology is well established, and abnormalities are found in multiple disorders, the mechanisms that mediate t-tubule growth are unknown. We show that the actomyosin cortex beneath the plasma membrane, regulated by Arp2/3 complexes containing Arpc5, acts as a gatekeeper for the membrane availability required for t-tubule growth. Enlarged t-tubules are formed upon disruption of Arpc5, impairing the synchronisation between plasma membrane depolarization and calcium release. Additionally, ablation of Arpc5 postnatally in myofibers results in muscle fatigue and t-tubule abnormalities, as observed in muscle disorders. We propose that the actomyosin cortex impacts muscle function, offering a potential pathophysiological mechanism for muscle disorders.

Main text: The contractile properties of skeletal muscle are essential for body movement, posture, and breathing. These vital functions are affected by multiple disorders and decline with age (*1*). Sarcomeres are the contractile units of muscle cells and contract synchronously upon calcium release from the endoplasmic reticulum (ER), also known as sarcoplasmic reticulum. Muscle contraction is initiated at the neuromuscular junction by local depolarisation of the plasma membrane, which propagates throughout the muscle cell (myofiber) surface (*2*). Since myofibers are the longest and thickest cells in the human body, the depolarisation signal is propagated throughout their entire volume via plasma membrane invaginations called transverse tubules (t-tubules) that surround sarcomeres (*3*–*5*). These t-tubules form membrane contact sites with two adjacent endoplasmic reticulum compartments, creating a structure termed a triad. Depolarisation of the t-tubule membrane triggers calcium release from the ER at the triads, a phenomenon termed excitation-contraction coupling (EC-coupling). Disruptions in triad assembly and morphology result in EC-coupling abnormalities, characteristic of multiple muscle disorders (*6*).

During mammalian development, a network of t-tubules emerges in myofibers in the embryo and becomes organized transversely only after birth (*7*). T-tubule biogenesis is initiated from plasma membrane invaginations mediated by Amphiphysin 2 (Bin1), a BAR domain protein, and caveolin-3-containing caveolae (*8*). Endosomal membrane traffic has been implicated in t-tubule network formation and maintenance (*3*, *9*). In adults, t-tubules have a surface area approximately seven times that of the myofiber plasma membrane, however it remains unclear how t-tubules grow (*10*).

The plasma membrane is tethered to the actomyosin cortex by membrane-to-cortex attachment proteins such as ezrin, radixin and moesin (ERM) family, that impact membrane remodelling (*11*–*13*). The actomyosin cortex consists of both linear and branched actin filaments, the latter of which is nucleated by the Arp2/3 complex composed of 7 evolutionarily conserved subunits (*14*, *15*). Notably, three Arp2/3 subunits are encoded by more than one gene in mammals, yielding Arp2/3 complexes with different properties (*16*–*18*). This diversity generates Arp2/3 complexes that appear to be tailored for specific cellular functions, including cell migration, viral transport, or T-cell activation (*16*, *19*, *20*). In skeletal muscle, we previously demonstrated that Arp2/3 complexes containing Arpc5L drive nuclei positioning to the periphery of myofiber by promoting desmin-dependent myofibril crosslinking to generate centripetal forces on the nucleus (*21*). In contrast, Arp2/3 complexes containing Arpc5 plays an essential role in triad organisation by an unknown mechanism. Here we investigated how Arpc5-containing Arp2/3 complexes are involved in t-tubule and triad organisation.

72 ## Results

73 ### Inhibition of the Arp2/3 complex promotes t-tubule growth

74 To understand how the t-tubule network is established in myofibers, we first
75 evaluated t-tubule dynamics. For this, we incubated myofibers isolated from adult mice
76 or *in vitro* developing myofibers with a plasma membrane dye (CellMask) to label t-
77 tubules, and performed time-lapse microscopy (*7*). We observed that t-tubules exhibit
78 growing and shrinking movements in both isolated myofibers and developing myofibers
79 (Fig. 1A and 1B, Movie S1-S2). T-tubule growth was independent of t-tubule-ER contacts
80 (fig. S1, Movie S3).

81 We previously found that triad organisation during myofiber formation depends
82 on the Arp2/3 complex (*21*). Building upon this observation, we hypothesised that the
83 Arp2/3 complex is required for t-tubule growth. We treated developing myofibers with the
84 Arp2/3 inhibitor CK666, and contrary to our hypothesis, there was a significant increase
85 in the number of growing t-tubules (Fig. 1C, Movie S4). T-tubule formation is mediated
86 by Bin1 and its overexpression is sufficient to induce plasma membrane tubulation (*8*,
87 *22*, *23*). Stable expression of GFP-Bin1 in C2C12 myoblasts (GFP-Bin1 myoblasts)
88 resulted in dynamic tubules similar to those in developing myofibers (Movie S5).
89 Moreover, treatment with CK666 also increased the number of growing tubules (Fig. 1D;
90 Movie S5). Together, these results show that Arp2/3 inhibition promotes t-tubule and
91 membrane tubule growth.

92 ### F-Actin does not accumulate near growing tubules

93 Actin cytoskeleton and Arp2/3 complex can modulate membrane tubulation in
94 multiple organelles (*24*). To investigate whether actin was enriched at growing tubules
95 we imaged actin filaments (F-actin) using LifeAct-mCherry or mScarlet-Utrophin on
96 membrane tubules formed in GFP-Bin1 myoblasts. We did not observe F-actin
97 enrichment during tubule growth (fig. S2 A-D; Movie S6 and S7). We also performed
98 cryo-correlative Light and Electron Microscopy (cryo-CLEM) and cryo-electron
99 tomography (cryo-ET) of GFP-Bin1 myoblasts in regions containing tubules (fig. S2E-I,
100 S3, S4). We observed unbranched F-actin forming bundles or meshes throughout the
101 different volumes (fig. S2H, I, S4A and S4B, Movie S8-S10). However, analysis of the
102 volume across different z positions revealed no distinct arrangement of actin filaments
103 near the tubules when compared to other cytoplasmic regions (fig. S2I, S4C-J).
104 Importantly, we observed very few actin branches around tubules (fig. S2I), and they
105 were not more abundant when compared to other regions of the cytoplasm (fig. S4C-J).

106 This stands in contrast to clathrin-mediated endocytosis, where branched actin is
107 enriched near the endocytic membrane (*25*, *26*). Overall, these data suggest that
108 branched F-actin does not accumulate near growing t-tubules, leading us to explore
109 contributions by the Arp2/3 network to t-tubule dynamics elsewhere in the cell.

110 **The actomyosin cortex limits t-tubule growth**

111 During myofiber development, plasma membrane must be available to form t-
112 tubules. Plasma membrane is regulated by the underlying cell cortex consisting of an
113 actomyosin network linked to the plasma membrane by the ezrin-radixin-moesin proteins
114 (ERM) (*11*, *13*). Since the cortical actin is regulated by the Arp2/3 complex, we
115 hypothesised that perturbing the actomyosin cortex leads to increased membrane
116 availability required for t-tubule growth (*15*, *27*, *28*). To test this hypothesis, we interfered
117 with actomyosin cortex by inhibiting myosin-2, using para-aminoblebbistatin
118 (blebbistatin), and quantified the number of growing tubules before and after treatment
119 (*29*, *30*). Blebbistatin treatment of GFP-Bin1 myoblasts or developing myofibers led to a
120 significant increase in the number of growing tubules (Fig. 1E and 1F; Movie S11 and
121 S12). We also induced an excess of plasma membrane by a rapid reduction of cell
122 volume with a hyperosmotic shock (*31*). Quantification of the number of growing tubules
123 before and after osmotic shock revealed an increase in the number of growing tubules
124 (Fig. 1G and 1H, Movie S13 and S14). In addition, the interference of membrane to
125 cortex attachment with NSC668394, an ezrin phosphorylation inhibitor (*32*) also results
126 in an increase in the number of growing tubules (Fig. 1I and 1J; Movie S15 and S16).
127 Conversely, overexpression of a constitutively active form of Ezrin (CA-Ezrin) (*33*)
128 reduces the number of growing t-tubules (Fig. 1J, graph). Importantly, cells expressing
129 CA-Ezrin had fewer growing t-tubules when compared to those with WT-Ezrin (Fig. 1J,
130 graph). Together, these findings suggest that the actomyosin cortex functions as a
131 regulatory gatekeeper in the growth of t-tubules.

132 **Arpc5 limits t-tubule growth through the actomyosin cortex**

133 We showed that Arp2/3 complexes containing Arpc5 are involved in triad
134 organization (*15*, *21*, *27*). Therefore, we hypothesized that Arpc5 role in triad
135 organization relates to its function in regulating cortical actin-mediated t-tubule growth.
136 To test if Arpc5 had a role in t-tubule growth, we performed knock-down (KD)
137 experiments with siRNA targeting Arpc5 in GFP-Bin1 myoblasts and developing
138 myofibers (fig. S5). We found that depletion of Arpc5, results in significantly more
139 growing tubules in GFP-Bin1 myoblasts and t-tubules in developing myofibers when
140 compared to controls (Fig. 2A and 2B; Movie S17 and S18). Next we evaluated the role

141 of Arpc5 on the actomyosin cortex in developing myofibers. We found that non-muscle-
142 myosin2B (NM-Myo2B) localizes as foci at the membrane that were reduced upon Arpc5
143 depletion (Fig. 2C and 2D). In addition, the levels of actin ERM proteins (pERM) were
144 also reduced and its distribution was more heterogeneous following Arpc5 KD (Fig. 2E-
145 G). Finally we assessed muscle cells' nanoscale topology using Atomic Force
146 Microscopy (AFM) and found that depletion of Arpc5 leads to an increase in membrane
147 roughness (Fig. 2H). These data suggests that depletion of Arpc5 impacts the
148 actomyosin cortex and the membrane to cortex attachment in developing myofibers (Fig.
149 2I).

150 **Arpc5 depletion leads to enlarged t-tubule clusters and asynchronous EC-**
151 **coupling**

152 During myofiber development, t-tubules form two-sided connections with the ER,
153 establishing triads that become transversely organised (*3–5*). Since loss of Arpc5
154 impacted triad organisation (*21*), we investigated the role of Arpc5 in the t-tubule network
155 in more differentiated myofibers (*21*, *34*). In control conditions, we observed transversely
156 and longitudinally aligned t-tubules which are evenly distributed throughout the myofiber
157 (Fig. 3A). In contrast, in Arpc5 KD myofibers, t-tubules formed clusters (Fig. 3A-C). Using
158 joint-deconvolution Airyscan microscopy, we found that the clusters are composed of
159 enlarged t-tubules (Fig. 3D). Transmission electron microscopy (TEM) of differentiated
160 myofibers confirmed a higher proportion of enlarged t-tubules in Arpc5 KD myofibers
161 (Fig. 3E and 3F). Furthermore, we observed a reduction of triads in Arpc5 KD compared
162 to the control both using TEM and fluorescence microscopy of Junctophilin-1 (JPH1)
163 puncta, a marker of triads, (Fig. 3E green arrowheads, 3G-I). Together, these results
164 show that Arpc5 depletion impacts t-tubule and triad morphology.
165 As triads are fundamental for EC-coupling, we assessed the impact of the loss
166 of Arpc5 on calcium release and cell contraction in differentiated myofibers (Fig. 3J). We
167 found that myofibers depleted for Arpc5, exhibited abnormalities in calcium transients,
168 which were not synchronised with the electrical stimulation, when compared to WT
169 myofibers (Fig. 3K and 3L). We then performed single-myofiber contraction tracing (Fig.
170 3M) and found that myofibers could still contract when Arpc5 is depleted (Fig. 3M and
171 3N). However, there was a dramatic asynchrony between electrical stimulation and
172 myofiber contraction (Fig. 3M and 3O). These results highlight the role of Arpc5
173 containing Arp2/3 complexes and limiting t-tubule overgrowth in EC-coupling for muscle
174 contraction.
175
176

177 **Arpc5 is associated muscle function during postnatal development in mice**

178 Our in vitro myofibers are differentiated up to a stage equivalent to postnatal day
179 1 myofibers, which have nuclei at the periphery, organized transverse triads, and a
180 network of transverse and longitudinal t-tubules (*35*, *36*). However, the t-tubule
181 transverse network only becomes fully established during the first weeks of postnatal
182 development in mice (*7*, *36*). To determine if Arpc5 has a role to further mature t-tubules
183 and triads, we investigated mouse skeletal muscle postnatal development. As
184 constitutive Arpc5 knockout mouse model is embryonically lethal (*37*), we used a
185 tamoxifen-inducible, skeletal muscle-specific Arpc5 knockout model (Arpc5$^{-/-}$, Fig. 4A)
186 (*38*). To induce Arpc5 knockout during postnatal development, we administered 4OH-
187 tamoxifen immediately after birth - postnatal (P) days 1, 2 and 3 - and characterized the
188 neonatal Arpc5$^{-/-}$ mice at P7. Arpc5 protein levels were significantly decreased when
189 compared to Arpc5$^{fl/fl}$ (Arpc5^{WT}) (Fig. 4B and 4C). We performed TEM on longitudinal
190 sections of hind limb muscle and found that the plasma membrane of Arpc5$^{-/-}$ mice was
191 more irregular than Arpc5^{WT} (Fig. 4D). Mature transverse t-tubules were decreased,
192 whereas diagonal and longitudinal t-tubules did not change, suggesting that Arpc5 is
193 also involved in t-tubule maturation that occurs postnatally. We also observed an
194 increase of enlarged t-tubules in triads (Fig. 4E-G). Additionally, we found no difference
195 in the number of triads between Arpc5^{WT} and Arpc5$^{-/-}$ mice (Fig. 4H). Finally, structural
196 alterations described above were associated with functional impairments in Arpc5$^{-/-}$
197 skeletal muscle physiology, as hind limb suspension tests revealed increased fatigue
198 and muscle weakness in Arpc5$^{-/-}$ mice (Fig. 4I). These findings unveil the role of Arpc5
199 in t-tubule maturation and muscle function during postnatal development.
200

Conclusions: T-tubules and their connection with the endoplasmic reticulum to form triads are fundamental for muscle contraction and are disrupted in multiple muscle disorders (*6*). We now show that the actomyosin cortex, regulated by Arpc5-containing Arp2/3 complexes, acts as a gatekeeper for membrane availability required for t-tubule growth. This is essential for ensuring proper myofiber development and muscle function and provides a novel pathophysiological mechanism for muscle disorders with impaired triad function.

Our observations reveal that the destabilization of the actomyosin cortex releases plasma membrane, enabling t-tubule extension. Membrane tubulation has also been observed following stretch release in adherent cells, suggesting that membrane release facilitates tubule formation (*39*). In addition, elegant experiments using giant unilamellar vesicles have demonstrated that membrane release alone, induced by a reduction in vesicle volume, can drive inward tubulation, mimicking t-tubule formation without the need for external forces (*40*). Importantly, we did not observe enrichment of actin or accumulation of branched actin near growing t-tubules. While we cannot exclude the involvement of external forces, our data does not support a requirement for actin-mediated force generation in t-tubule growth. Bin1 has also been shown to induce membrane tubulation independently of actin (*41*). Bin1, along with proteins such as dynamin-2, likely contributes to t-tubule growth by stabilizing membrane curvature, in synergy with the mechanism we identify (*41*, *42*).

Our findings support a model in which limiting t-tubule growth is essential for proper triad formation and synchronized muscle contraction. Excessive t-tubule growth may disrupt membrane contacts with the endoplasmic reticulum, impairing triad assembly and function. Postnatal loss of Arpc5 results in t-tubule abnormalities that might lead to the observed muscle fatigue, highlighting its role in maintaining t-tubule architecture. During postnatal development, t-tubules and triads undergo spatial consolidation into a transverse orientation and our results suggest that actomyosin cortex regulation has a role in this process (*7*, *36*). T-tubule overgrowth and triad abnormalities have been observed in aged human muscle (*43*). Moreover, several muscle disorders characterized by defective triads, including those involving mutations in Mitsugumin 25, Dysferlin, Myotubularin, and Dynamin-2, also exhibit excessive t-tubule clustering (*3*, *6*). Thus, the mechanism that regulates t-tubule growth that we identify may be a common therapeutic target for these disorders.

References and Notes

1. J. J. Dowling, C. C. Weihl, M. J. Spencer, Molecular and cellular basis of genetically inherited skeletal muscle disorders. *Nat. Rev. Mol. Cell Biol.* **22**, 713–732 (2021).

2. C. Franzini-Armstrong, The relationship between form and function throughout the history of excitation–contraction coupling. *J. Gen. Physiol.* **150**, 189–210 (2018).

3. L. Al-Qusairi, J. Laporte, T-tubule biogenesis and triad formation in skeletal muscle and implication in human diseases. *Skelet. Muscle* **1**, 26 (2011).

4. K. Kawaguchi, N. Fujita, Shaping transverse-tubules: central mechanisms that play a role in the cytosol zoning for muscle contraction. *J. Biochem. (Tokyo)* **175**, 125–131 (2024).

5. K. R. Porter, G. E. Palade, Studies on the endoplasmic reticulum. III. Its form and distribution in striated muscle cells. *J. Biophys. Biochem. Cytol.* **3**, 269–300 (1957).

6. J. J. Dowling, M. W. Lawlor, R. T. Dirksen, Triadopathies: An Emerging Class of Skeletal Muscle Diseases. *Neurotherapeutics* **11**, 773–785 (2014).

7. H. Takekura, B. E. Flucher, C. Franzini-Armstrong, Sequential docking, molecular differentiation, and positioning of T-Tubule/SR junctions in developing mouse skeletal muscle. *Dev. Biol.* **239**, 204–214 (2001).

8. E. Lemerle, J. Lainé, M. Benoist, G. Moulay, A. Bigot, C. Labasse, A. Madelaine, A. Canette, P. Aubin, J.-M. Vallat, N. B. Romero, M. Bitoun, V. Mouly, I. Marty, B. Cadot, L. Picas, S. Vassilopoulos, Caveolae and Bin1 form ring-shaped platforms for T-tubule initiation. *eLife* **12**, e84139 (2023).

9. T. E. Hall, N. Martel, N. Ariotti, Z. Xiong, H. P. Lo, C. Ferguson, J. Rae, Y.-W. Lim, R. G. Parton, In vivo cell biological screening identifies an endocytic capture mechanism for T-tubule formation. *Nat. Commun.* **11**, 3711 (2020).

10. L. D. Peachey, THE SARCOPLASMIC RETICULUM AND TRANSVERSE TUBULES OF THE FROG'S SARTORIUS. *J. Cell Biol.* **25**, 209–231 (1965).

11. P. Chugh, E. K. Paluch, The actin cortex at a glance. *J. Cell Sci.* **131**, jcs186254 (2018).

12. A. Jawahar, J. Vermeil, J. Heuvingh, O. du Roure, M. Piel, The third dimension of the actin cortex. *Curr. Opin. Cell Biol.* **89**, 102381 (2024).

13. T. M. Svitkina, Actin Cell Cortex: Structure and Molecular Organization. *Trends Cell Biol.* **30**, 556–565 (2020).

14. K. G. Campellone, N. M. Lebek, V. L. King, Branching out in different directions: Emerging cellular functions for the Arp2/3 complex and WASP-family actin nucleation factors. *Eur. J. Cell Biol.* **102**, 151301 (2023).

15. L. Cao, A. Yonis, M. Vaghela, E. H. Barriga, P. Chugh, M. B. Smith, J. Maufront, G. Lavoie, A. Méant, E. Ferber, M. Bovellan, A. Alberts, A. Bertin, R. Mayor, E. K. Paluch, P. P. Roux, A. Jégou, G. Romet-Lemonne, G. Charras, SPIN90

associates with mDia1 and the Arp2/3 complex to regulate cortical actin organization. *Nat. Cell Biol.* **22**, 803–814 (2020).

16. J. V. G. Abella, C. Galloni, J. Pernier, D. J. Barry, S. Kjær, M.-F. Carlier, M. Way, Isoform diversity in the Arp2/3 complex determines actin filament dynamics. *Nat. Cell Biol.* **18**, 76–86 (2016).

17. L. Cao, S. Huang, A. Basant, M. Mladenov, M. Way, CK-666 and CK-869 differentially inhibit Arp2/3 iso-complexes. *EMBO Rep.*, 1–19 (2024).

18. C. Galloni, D. Carra, J. V. G. Abella, S. Kjær, P. Singaravelu, D. J. Barry, N. Kogata, C. Guérin, L. Blanchoin, M. Way, MICAL2 enhances branched actin network disassembly by oxidizing Arp3B-containing Arp2/3 complexes. *J. Cell Biol.* **220**, e202102043 (2021).

19. F. Fäßler, M. G. Javoor, J. Datler, H. Döring, F. W. Hofer, G. Dimchev, V.-V. Hodirnau, J. Faix, K. Rottner, F. K. M. Schur, ArpC5 isoforms regulate Arp2/3 complex-dependent protrusion through differential Ena/VASP positioning. *Sci. Adv.* **9**, eadd6495 (2023).

20. L. Sadhu, N. Tsopoulidis, M. Hasanuzzaman, V. Laketa, M. Way, O. T. Fackler, ARPC5 isoforms and their regulation by calcium-calmodulin-N-WASP drive distinct Arp2/3-dependent actin remodeling events in CD4 T cells. *eLife* **12**, e82450 (2023).

21. W. Roman, J. P. Martins, F. A. Carvalho, R. Voituriez, J. V. G. Abella, N. C. Santos, B. Cadot, M. Way, E. R. Gomes, Myofibril contraction and cross-linking drive nuclear movement to the periphery of skeletal muscle. *Nat. Cell Biol.* **19**, 1189–1201 (2017).

22. E. Lee, M. Marcucci, L. Daniell, M. Pypaert, O. A. Weisz, G.-C. Ochoa, K. Farsad, M. R. Wenk, P. De Camilli, Amphiphysin 2 (Bin1) and T-tubule biogenesis in muscle. *Science* **297**, 1193–1196 (2002).

23. A.-S. Nicot, A. Toussaint, V. Tosch, C. Kretz, C. Wallgren-Pettersson, E. Iwarsson, H. Kingston, J.-M. Garnier, V. Biancalana, A. Oldfors, J.-L. Mandel, J. Laporte, Mutations in amphiphysin 2 (BIN1) disrupt interaction with dynamin 2 and cause autosomal recessive centronuclear myopathy. *Nat. Genet.* **39**, 1134–1139 (2007).

24. A. Allard, R. Lopes dos Santos, C. Campillo, Remodelling of membrane tubules by the actin cytoskeleton. *Biol. Cell* **113**, 329–343 (2021).

25. A. Collins, A. Warrington, K. A. Taylor, T. Svitkina, Structural Organization of the Actin Cytoskeleton at Sites of Clathrin-Mediated Endocytosis. *Curr. Biol.* **21**, 1167–1175 (2011).

26. D. Serwas, M. Akamatsu, A. Moayed, K. Vegesna, R. Vasan, J. M. Hill, J. Schöneberg, K. M. Davies, P. Rangamani, D. G. Drubin, Mechanistic insights into actin force generation during vesicle formation from cryo-electron tomography. *Dev. Cell* **57**, 1132-1145.e5 (2022).

27. M. Bovellan, Y. Romeo, M. Biro, A. Boden, P. Chugh, A. Yonis, M. Vaghela, M. Fritzsche, D. Moulding, R. Thorogate, A. Jégou, A. J. Thrasher, G. Romet-Lemonne, P. P. Roux, E. K. Paluch, G. Charras, Cellular control of cortical actin

nucleation. *Curr. Biol. CB* **24**, 1628–1635 (2014).

28. M. Fritzsche, C. Erlenkämper, E. Moeendarbary, G. Charras, K. Kruse, Actin kinetics shapes cortical network structure and mechanics. *Sci. Adv.* **2**, e1501337 (2016).

29. V. Laplaud, N. Levernier, J. Pineau, M. S. Roman, L. Barbier, P. J. Sáez, A.-M. Lennon-Duménil, P. Vargas, K. Kruse, O. du Roure, M. Piel, J. Heuvingh, Pinching the cortex of live cells reveals thickness instabilities caused by myosin II motors. *Sci. Adv.* **7**, eabe3640 (2021).

30. B. H. Várkuti, M. Képiró, I. Á. Horváth, L. Végner, S. Ráti, Á. Zsigmond, G. Hegyi, Z. Lenkei, M. Varga, A. Málnási-Csizmadia, A highly soluble, non-phototoxic, non-fluorescent blebbistatin derivative. *Sci. Rep.* **6**, 26141 (2016).

31. C. Roffay, G. Molinard, K. Kim, M. Urbanska, V. Andrade, V. Barbarasa, P. Nowak, V. Mercier, J. García-Calvo, S. Matile, R. Loewith, A. Echard, J. Guck, M. Lenz, A. Roux, Passive coupling of membrane tension and cell volume during active response of cells to osmosis. *Proc. Natl. Acad. Sci.* **118**, e2103228118 (2021).

32. G. Bulut, S.-H. Hong, K. Chen, E. M. Beauchamp, S. Rahim, G. W. Kosturko, E. Glasgow, S. Dakshanamurthy, H.-S. Lee, I. Daar, J. A. Toretsky, C. Khanna, A. Üren, Small molecule inhibitors of ezrin inhibit the invasive phenotype of osteosarcoma cells. *Oncogene* **31**, 269–281 (2012).

33. M. Fritzsche, R. Thorogate, G. Charras, Quantitative analysis of ezrin turnover dynamics in the actin cortex. *Biophys. J.* **106**, 343–353 (2014).

34. S. Falcone, W. Roman, K. Hnia, V. Gache, N. Didier, J. Lainé, F. Auradé, I. Marty, I. Nishino, N. Charlet-Berguerand, N. B. Romero, G. Marazzi, D. Sassoon, J. Laporte, E. R. Gomes, N-WASP is required for Amphiphysin-2/BIN1-dependent nuclear positioning and triad organization in skeletal muscle and is involved in the pathophysiology of centronuclear myopathy. *EMBO Mol. Med.* **6**, 1455–1475 (2014).

35. B. E. Flucher, S. B. Andrews, M. P. Daniels, Molecular organization of transverse tubule/sarcoplasmic reticulum junctions during development of excitation-contraction coupling in skeletal muscle. *Mol. Biol. Cell* **5**, 1105–1118 (1994).

36. C. Franzini-Armstrong, Simultaneous maturation of transverse tubules and sarcoplasmic reticulum during muscle differentiation in the mouse. *Dev. Biol.* **146**, 353–363 (1991).

37. E. Sindram, A. Caballero-Oteyza, N. Kogata, S. Chor Mei Huang, Z. Alizadeh, L. Gámez-Díaz, M. R. Fazlollhi, X. Peng, B. Grimbacher, M. Way, M. Proietti, ARPC5 deficiency leads to severe early-onset systemic inflammation and mortality. *Dis. Model. Mech.* **16**, dmm050145 (2023).

38. J. J. McCarthy, R. Srikuea, T. J. Kirby, C. A. Peterson, K. A. Esser, Inducible Cre transgenic mouse strain for skeletal muscle-specific gene targeting. *Skelet. Muscle* **2**, 8 (2012).

39. A. J. Kosmalska, L. Casares, A. Elosegui-Artola, J. J. Thottacherry, R. Moreno-Vicente, V. González-Tarragó, M. Á. del Pozo, S. Mayor, M. Arroyo, D. Navajas,

X. Trepat, N. C. Gauthier, P. Roca-Cusachs, Physical principles of membrane remodelling during cell mechanoadaptation. *Nat. Commun.* **6**, 7292 (2015).

40. Y. Li, R. Lipowsky, R. Dimova, Membrane nanotubes induced by aqueous phase separation and stabilized by spontaneous curvature. *Proc. Natl. Acad. Sci.* **108**, 4731–4736 (2011).

41. L. Picas, J. Viaud, K. Schauer, S. Vanni, K. Hnia, V. Fraisier, A. Roux, P. Bassereau, F. Gaits-Iacovoni, B. Payrastre, J. Laporte, J.-B. Manneville, B. Goud, BIN1/M-Amphiphysin2 induces clustering of phosphoinositides to recruit its downstream partner dynamin. *Nat. Commun.* **5**, 5647 (2014).

42. V. M. Lionello, C. Kretz, E. Edelweiss, C. Crucifix, R. Gómez-Oca, N. Messaddeq, S. Buono, P. Koebel, X. Massana Muñoz, N. Diedhiou, B. S. Cowling, M. Bitoun, J. Laporte, BIN1 modulation in vivo rescues dynamin-related myopathy. *Proc. Natl. Acad. Sci.* **119**, e2109576119 (2022).

43. S. Boncompagni, L. d'Amelio, S. Fulle, G. Fanò, F. Protasi, Progressive Disorganization of the Excitation–Contraction Coupling Apparatus in Aging Human Skeletal Muscle as Revealed by Electron Microscopy: A Possible Role in the Decline of Muscle Performance. *J. Gerontol. Ser. A* **61**, 995–1008 (2006).

44. M. R. Pimentel, S. Falcone, B. Cadot, E. R. Gomes, In Vitro Differentiation of Mature Myofibers for Live Imaging. *J. Vis. Exp. JoVE*, 55141 (2017).

45. D. N. Feather-Schussler, T. S. Ferguson, A Battery of Motor Tests in a Neonatal Mouse Model of Cerebral Palsy. *J. Vis. Exp. JoVE*, 53569 (2016).

46. C. S. Janota, A. Pinto, A. Pezzarossa, P. Machado, J. Costa, P. Campinho, C. A. Franco, E. R. Gomes, Shielding of actin by the endoplasmic reticulum impacts nuclear positioning. *Nat. Commun.* **13**, 2763 (2022).

47. A. O. Chertkova, M. Mastop, M. Postma, N. Van Bommel, S. Van Der Niet, K. L. Batenburg, L. Joosen, T. W. J. Gadella, Y. Okada, J. Goedhart, Robust and Bright Genetically Encoded Fluorescent Markers for Highlighting Structures and Compartments in Mammalian Cells. doi: 10.1101/160374 (2017).

48. A. Fourest-Lieuvin, J. Rendu, A. Osseni, K. Pernet-Gallay, D. Rossi, S. Oddoux, J. Brocard, V. Sorrentino, I. Marty, J. Fauré, Role of triadin in the organization of reticulum membrane at the muscle triad. *J. Cell Sci.* **125**, 3443–3453 (2012).

49. A. the nonprofit plasmid Repository, AAV Production in HEK293T Cells. doi: dx.doi.org/10.17504/protocols.io.bawpifdn (2019).

50. A. the nonprofit plasmid Repository, AAV Purification by Iodixanol Gradient Ultracentrifugation. doi: dx.doi.org/10.17504/protocols.io.47jgzkn (2019).

51. J. Schindelin, I. Arganda-Carreras, E. Frise, V. Kaynig, M. Longair, T. Pietzsch, S. Preibisch, C. Rueden, S. Saalfeld, B. Schmid, J.-Y. Tinevez, D. J. White, V. Hartenstein, K. Eliceiri, P. Tomancak, A. Cardona, Fiji: an open-source platform for biological-image analysis. *Nat. Methods* **9**, 676–682 (2012).

52. T. Ferreira, K. Miura, B. Chef, J. Eglinger, *Scripts: BAR 1.1.6* (Zenodo, 2015; https://zenodo.org/records/28838).

53. J. W. Pylvänäinen, R. F. Laine, B. M. S. Saraiva, S. Ghimire, G. Follain, R. Henriques, G. Jacquemet, Fast4DReg – fast registration of 4D microscopy datasets. *J. Cell Sci.* **136**, jcs260728 (2023).

54. D. Ershov, M.-S. Phan, J. W. Pylvänäinen, S. U. Rigaud, L. Le Blanc, A. Charles-Orszag, J. R. W. Conway, R. F. Laine, N. H. Roy, D. Bonazzi, G. Duménil, G. Jacquemet, J.-Y. Tinevez, TrackMate 7: integrating state-of-the-art segmentation algorithms into tracking pipelines. *Nat. Methods* **19**, 829–832 (2022).

55. J. Zivanov, J. Otón, Z. Ke, A. von Kügelgen, E. Pyle, K. Qu, D. Morado, D. Castaño-Díez, G. Zanetti, T. A. M. Bharat, J. A. G. Briggs, S. H. W. Scheres, A Bayesian approach to single-particle electron cryo-tomography in RELION-4.0. *eLife* **11**, e83724 (2022).

56. S. Q. Zheng, E. Palovcak, J.-P. Armache, K. A. Verba, Y. Cheng, D. A. Agard, MotionCor2: anisotropic correction of beam-induced motion for improved cryo-electron microscopy. *Nat. Methods* **14**, 331–332 (2017).

57. A. Rohou, N. Grigorieff, CTFFIND4: Fast and accurate defocus estimation from electron micrographs. *J. Struct. Biol.* **192**, 216–221 (2015).

58. T.-O. Buchholz, A. Krull, R. Shahidi, G. Pigino, G. Jékely, F. Jug, Content-aware image restoration for electron microscopy. *Methods Cell Biol.* **152**, 277–289 (2019).

59. Y.-T. Liu, H. Zhang, H. Wang, C.-L. Tao, G.-Q. Bi, Z. H. Zhou, Isotropic reconstruction for electron tomography with deep learning. *Nat. Commun.* **13**, 6482 (2022).

60. E. F. Pettersen, T. D. Goddard, C. C. Huang, E. C. Meng, G. S. Couch, T. I. Croll, J. H. Morris, T. E. Ferrin, UCSF ChimeraX: Structure visualization for researchers, educators, and developers. *Protein Sci. Publ. Protein Soc.* **30**, 70–82 (2021).

61. T.-W. Chen, T. J. Wardill, Y. Sun, S. R. Pulver, S. L. Renninger, A. Baohan, E. R. Schreiter, R. A. Kerr, M. B. Orger, V. Jayaraman, L. L. Looger, K. Svoboda, D. S. Kim, Ultrasensitive fluorescent proteins for imaging neuronal activity. *Nature* **499**, 295–300 (2013).

62. J. R. Kremer, D. N. Mastronarde, J. R. McIntosh, Computer Visualization of Three-Dimensional Image Data Using IMOD. *J. Struct. Biol.* **116**, 71–76 (1996).

63. M. Sébastien, P. Aubin, J. Brocard, J. Brocard, I. Marty, J. Fauré, Dynamics of triadin, a muscle-specific triad protein, within sarcoplasmic reticulum subdomains. *Mol. Biol. Cell* **31**, 261–272 (2020).

Acknowledgments: We thank all the members of the Gomes, Way and Moores laboratories for their continued support, scientific discussions and helpful comments on this work. We thank A.L. Sousa from the Electron Microscopy Facility at the Gulbenkian Institute for Molecular Medicine for her technical expertise, sample processing, and imaging of differentiated myofibers and postnatal myofibers by transmission electron microscopy. We also thank the Bioimaging Unit (funded by PPBI-POCI-01-0145-FEDER-022122) and the Rodent Facility of the Gulbenkian Institute for Molecular Medicine for their technical support. We thank N. Lukoyanova and S. Chen for electron microscope support and D. Houldershaw for computational support at Birkbeck. We finally thank the Molecular and Transgenic Tools Platform (MTTP) of Champalimaud Foundation for cloning and AAV production.

Funding information: This work was supported by the European Research Council (ERC) to Edgar Gomes, Carolyn Moores and Michael Way under the European Union's Horizon 2020 research and innovation programme (grant agreement No 810207). Michael Way is additionally supported by the Francis Crick Institute, which receives its core funding from Cancer Research UK (CC2096), the UK Medical Research Council (CC2096), and the Wellcome Trust (CC2096). Ana Raquel Pereira was supported by the Fundação para a Ciência e Tecnologia (CEECIND/CP1727/CT0003). We acknowledge Diamond Light Source for access and support of the cryo-EM facilities at the UK's national Electron Bio-imaging Centre (eBIC) funder proposal EM20287-56, funded by the Wellcome Trust, MRC and BBSRC. Sample optimization and cryo-CLEM experiments were conducted in the ISMB EM facility (Birkbeck College, University of London) with financial support from the Wellcome Trust (202679/Z/16/Z, 206166/Z/17/Z) and UKRI-Medical Research Council (MR/X013359/1). For the purpose of Open Access, the authors have applied a CC BY public copyright licence to any Author Accepted Manuscript version arising from this submission.

Author contributions: A.R.P. and A.R.S. carried out experiments and analysed data. T.L., J.L.F. and C.A.M designed the cryo-CLEM experiments, T.L and J.L.F. collected the cryo-ET data, T.L. performed the 3D reconstruction and segmentation the experiments and, T.L and C.A.M analysed the data. S.d.F. performed experiments with Arpc5 KO mice and analysed data. G.L. performed the t-tubule cluster imaging. I.F. generated GFP-Bin1 lentivirus expressing plasmid. F.A.C. and N.C.S. carried out AFM experiments. N.K. and M.W. provided unpublished data, tools, and animal models. A.R.P, A.R.S, and E.R.G designed experiments and wrote the manuscript with assistance from other authors. All authors participated in the critical review and revision of the manuscript. E.R.G, M.W and C.A.M supervised the project and secured funding.

Competing interests: The authors declare no competing interests.

Data and materials availability: All data are available in the main text or the supplementary materials.

Supplementary Materials

Materials and Methods

Supplementary Text

Figs. S1 to S5

Movies S1 to S18

Figures

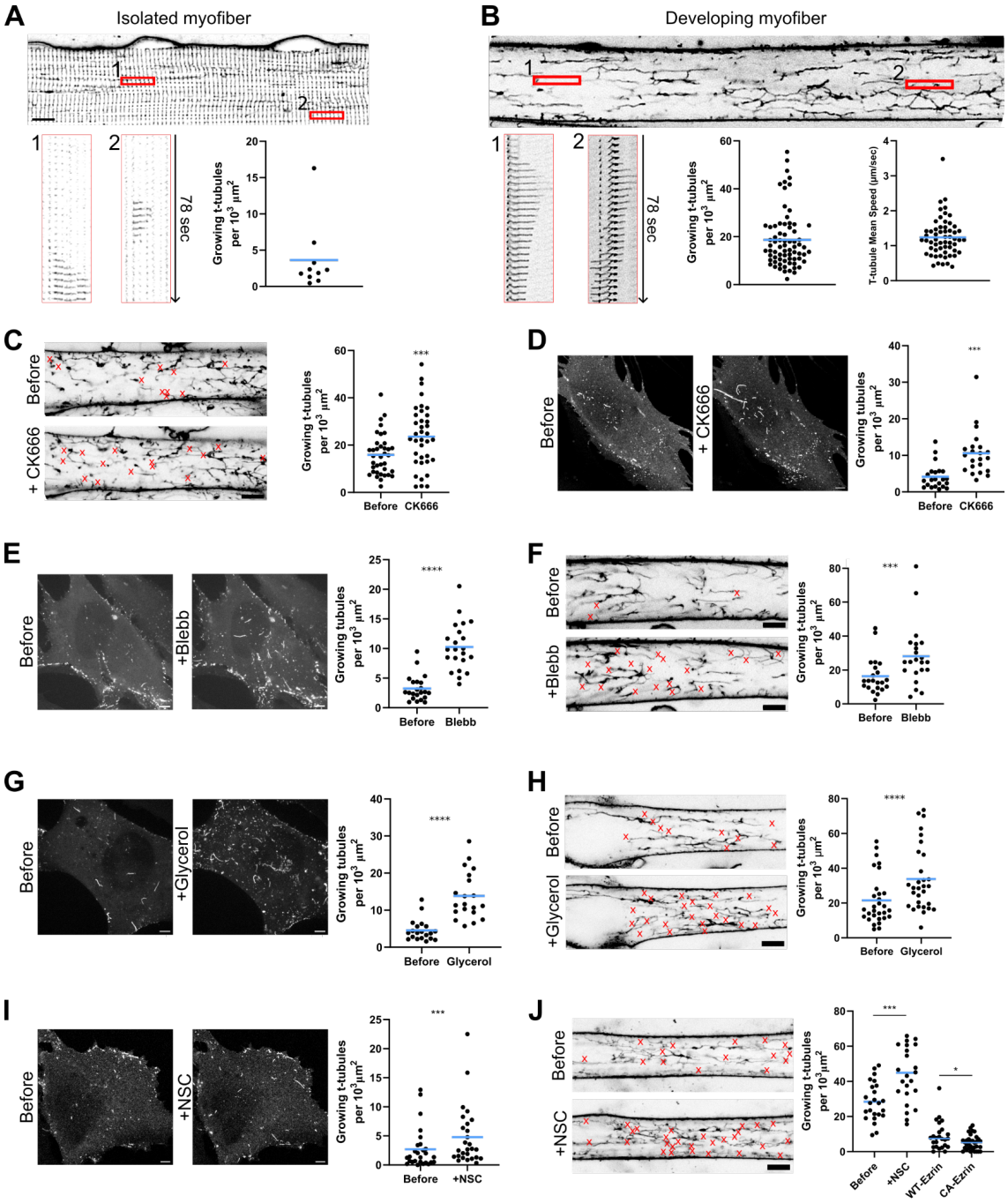

Fig. 1 – Actomyosin cortex limits t-tubule growth. (**A**) Top image corresponds to a timelapse snapshot of a mature isolated myofiber, stained with CellMask to label t-tubules and imaged by timelapse every 3 s for 2 min. Bottom image corresponds to kymographs from regions of interest (ROI) 1 and 2 of representative dynamic t-tubules. The plot represents the number of growing t-tubules per cell area during 2 min (N=10 isolated fibers, from three independent experiments). (**B**) Top image corresponds to a timelapse snapshot of an in vitro developing myofiber stained with CellMask to label t-tubules and imaged by timelapse every 3 sec for 2 min. At this stage of development (differentiation day 4), t-tubules are starting to form and have a longitudinal orientation. Bottom image corresponds to kymographs from ROIs 1 and 2 of representative dynamic t-tubules. The plots represent the number of growing t-tubules per cell area during 2 min (N=72 cells, from three independent experiments) and t-tubule growth mean speed (N=58 growing t-tubules, from three independent experiments). (**C**) Timelapse snapshots of in vitro developing myofibers (differentiation day 4) with CellMask labeled t-tubules before or after CK666

addition. Red X indicates the site of t-tubule growth during 2 min. The plot corresponds to the number of growing t-tubules per cell area during 2 min in the same myofibers before or after CK666 addition. Statistics: Wilcoxon test, p-value=0.0001; N=37 myofibers, results are from three independent experiments. (**D**) Timelapse snapshots of GFP-Bin1 before or after adding CK666. The plot corresponds to the number of growing tubules per cell during 2 min before or after adding CK666. Statistics: Wilcoxon test; N=22; results are from three independent experiments. (**E**) Timelapse snapshots of GFP-Bin1 myoblasts before or after para-aminoblebbistatin addition (Blebb). The plot corresponds to the number of growing tubules per cell area for 2 min before or after para-aminoblebbistatin addition. Statistics: Wilcoxon test; N=22 cells, results are from three independent experiments. (**F**) Timelapse snapshots of in vitro developing myofibers (differentiation day 4) with CellMask labeled t-tubules before or after para-aminoblebbistatin addition (Blebb). Red X indicates the site of t-tubule growth during 2 min. The plot corresponds to the number of growing t-tubules per cell area during 2 min in the same myofibers before or after para-aminoblebbistatin addition. Statistics: Wilcoxon test, p-value=0.0001; N=22 myofibers, results are from three independent experiments. (**G**) Timelapse snapshots of GFP-Bin1 myoblasts before or after glycerol addition. The plot corresponds to the number of growing tubules per cell area for 2 min before or after glycerol addition. Statistics: Wilcoxon test; N=20 cells, results are from three independent experiments. (**H**) Timelapse snapshots of in vitro developing myofibers (differentiation day 4) with CellMask labeled t-tubules before or after glycerol addition. Red X indicates the site of t-tubule growth during 2 min. The plot corresponds to the number of growing t-tubules per cell area during 2 min in the same myofibers before or after glycerol addition. Statistics: Wilcoxon test; N=30 myofibers, results are from three independent experiments. Scale bars 5 µm. (**I**) Timelapse snapshots of GFP-Bin1 myoblasts before or after NSC668394 (NSC). The plot corresponds to the number of growing tubules per cell area for 2 min before or after NSC addition. Statistics: Wilcoxon test; N=27 cells, results are from four independent experiments. (**J**) Timelapse snapshots of in vitro developing myofibers (differentiation day 4) with CellMask labeled t-tubules before or after NSC668394 addition (NSC). Red X indicates the site of t-tubule growth during 2 min. The plot corresponds to the number of growing t-tubules per cell area during 2 min in the same myofibers before NSC, after NSC, in cells expressing Ezrin-GFP (WT-Ezrin) or expressing constitutively active Ezrin-GFP (CA-Ezrin, T567D-GFP). Statistics: Before and After NSC: Paired t-test; N=24 myofibers. WT-Ezrin and CA-Ezrin: Mann-Whitney. WT-Ezrin N=25 and CA-Ezrin=33 myofibers. Results are from three independent experiments. Blue lines on all plots represent mean values. A-D, F-K scale bars 5 µm.

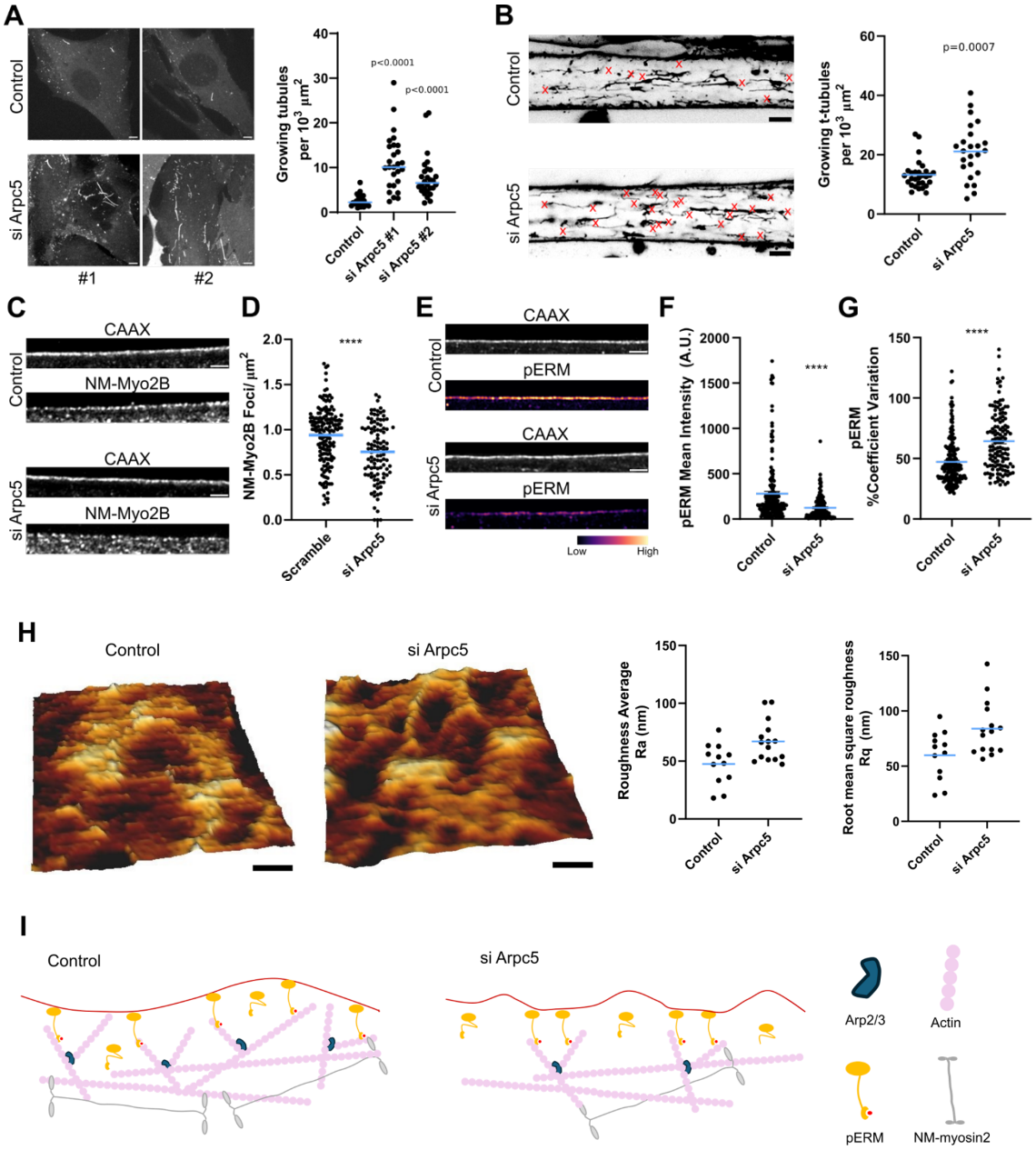

Fig. 2 – Arpc5 regulates cortical actin to limit t-tubule growth (A) Timelapse snapshots of GFP-Bin1 myoblasts transfected with scramble (Control) or Arpc5 (si Arpc5) siRNA. The plot corresponds to the number of growing tubules per cell area during 2 min. Statistics: Mann-Whitney; Control N=25; siArpC5#1 N=27 siArpC5#2 N=28. Results from three independent experiments. Scale bars 5 µm. (**B**) Timelapse snapshots of in vitro developing myofibers (differentiation day 4) with CellMask-labelled t-tubules from scramble (Control) or Arpc5 depleted (siArp5) myofibers. Red X indicates sites of t-tubule growth during 2 min. The plot corresponds to the number of growing t-tubules per cell area during 2 min. Statistics: Mann-Whitney, p-value=0.0007; Control N=29; siArpc5 N=24; results are from three independent experiments. Scale bars 5 µm. (**C**) Non-muscle myosin 2B (NM-Myo2B) staining in CAAX-GFP myofibers from scramble (Control) or depleted for Arpc5 (si Arpc5). Scale bar 2 µm. (**D**) Quantification of NM-myo2B foci per ROI area (µm^2). Each spot in the graph is the average number of identified NM-myo2B peaks per ROI segment area. Control N=164 ROIs, siArpc5 N=106. Statistics unpaired t-test, p-value <0.0001. Results are from three independent experiments. (**E**) PhosphoERM

545 (pERM) staining in CAAX-GFP myofibers from scramble (Control) or depleted for Arpc5 (siArpc5).
546 Scale bar 2 µm. (**F**) Plot corresponding to phosphoERM (pERM) mean intensity quantified over
547 consecutive 10 µm length segments at the plasma membrane (each spot is the average of the
548 pixel fluorescence intensity over the 10 µm segments). Control N=188 ROIs, siArpc5 N=148.
549 Statistics Mann-Whitney, p-value <0.0001. Results are from three independent experiments. (**G**)
550 Plot corresponding to the percentage of the coefficient of variation of phosphoERM signal
551 intensity (pERM) over consecutive 10 µm segments at the plasma membrane. Control N=188
552 ROIs, siArpc5 N=148. Statistics Mann-Whitney, p-value <0.0001 (**H**) Atomic Force Microscopy
553 (AFM) of developing myofibers. On the left a representative QI-mode height map image is shown
554 for control and si Arpc5 depleted myofibers. Scale bar 0.2 µm. Height scale 200 nm. Graphs show
555 the average roughness (Ra) and root mean square roughness (Rq) quantifications for surface
556 topography. Surface topographies of control cells (N=12) and Arpc5 KD cells (N=15) were
557 analyzed. Statistics Ra, unpaired t-test, p=0.0087. Statistics Rq, Student's unpaired t-test,
558 p=0.0143. Results are from three independent experiments (**I**) Schematic representation showing
559 that Arpc5 is important for maintaining the membrane to cortex attachment and membrane
560 flatness, gatekeeping membrane availability for t-tubule growth. Blue lines on all plots represent
561 mean values.

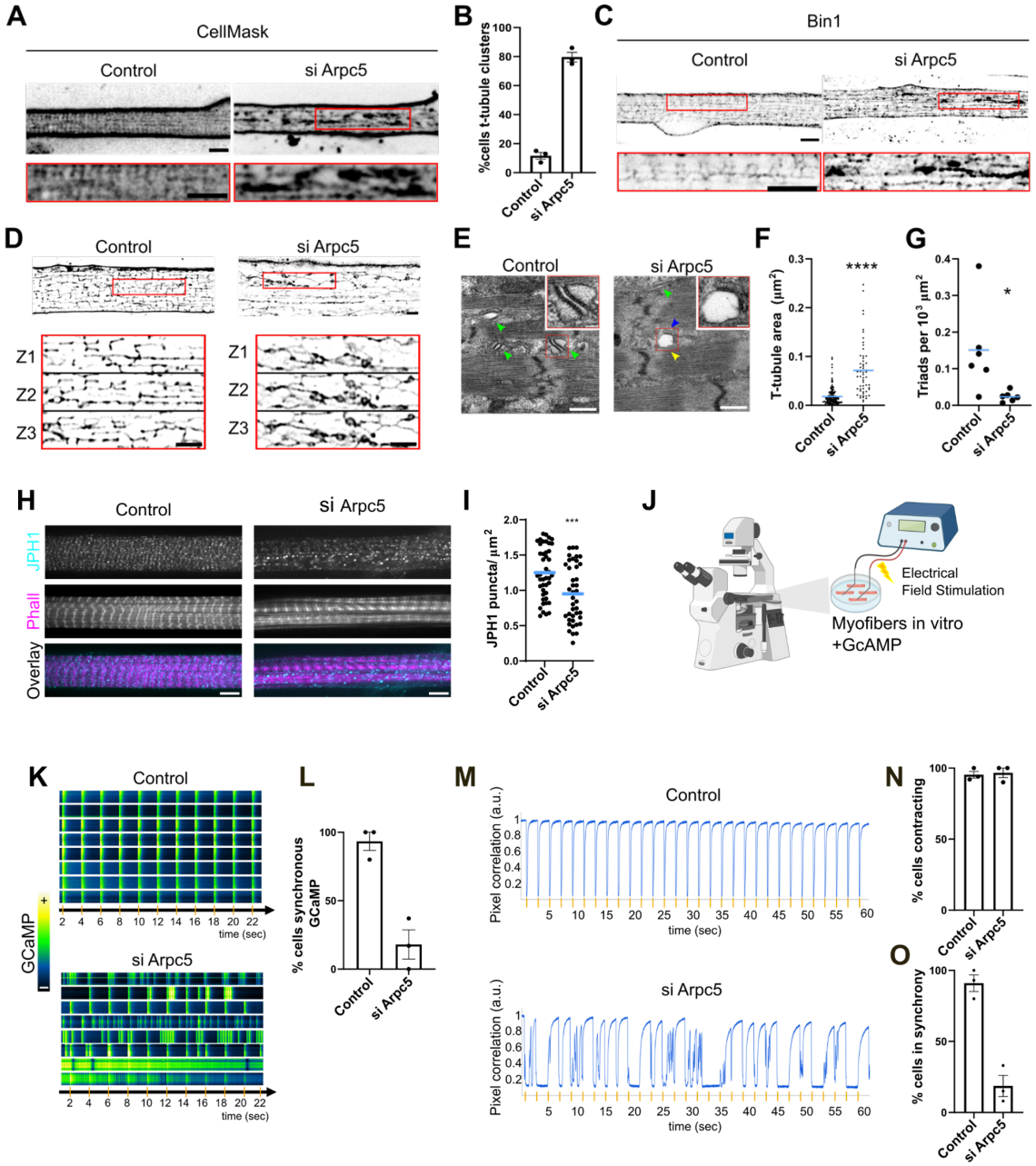

Fig. 3 - Arpc5 is involved in triad organization and synchronous EC-coupling (A) Representative images of CellMask labelled t-tubules from siRNA treated control (scramble) or Arpc5 (si Arpc5) myofibers (differentiation day 7). Magnifications corresponding to the red boxes are shown below each image. Scale bars 5 µm. (**B**) Quantification of the percentage of myofibers with t-tubule clusters. Control N=42 myofibers; si Arpc5 N= 41 myofibers, from three independent experiments. **(C)** Representative images of Bin1 immunostained t-tubules from siRNA treated control (scramble) or Arpc5 (si Arpc5) depleted myofibers (differentiation day 7). Magnifications corresponding to the red boxes are shown below each image. Scale bars 5 µm (**D**) Higher resolution reconstructions of Airyscan images using a Joint Deconvolution method. Magnification

576 Z slices corresponding to the red boxes are shown below of each image. Scale bars 2 µm. (**E**)
577 Transmission Electron Microscopy (TEM) of scramble (Control) or Arpc5 (si Arpc5) depleted
578 myofibers (differentiation day 7). Green arrowheads indicate triads (one t-tubule in contact with
579 two adjacent ER compartments). Blue arrows indicate t-tubules connected to the ER only on one
580 side, not forming a triad. Yellow arrowheads indicate enlarged t-tubules. Scale bars 500 nm.
581 Magnifications corresponding to the red ROIs are shown as insets, scale bars 100 nm. (**F**) Plot
582 representing the area of each t-tubule. Control N=162 t-tubules, si Arpc5 N=56 t-tubules. A total
583 of 6 cells were quantified per condition, two biological replicates. Mann-Whitney test ($p<0.0001$).
584 (**G**) Quantifications of the number of triads normalized for cell area (10^3 μm^2). Student's t-test
585 ($p=0.0286$). (**H**) Representative images of control (scramble), Arpc5 (si Arpc5) depleted myofibers
586 (differentiation day 7) immunostained for Junctophilin 1 (JPH1, cyan), Bin1 (Yellow); and stained
587 with phalloidin (Phall, magenta). Scale bars 5 µm. (**I**) Quantification of the number of Junctophilin
588 1 (JPH1) puncta per μm^2 in scramble (Control) or Arpc5 (si Arpc5) depleted myofibers. Statistics:
589 Mann-Whitney statistical test, siArpc5 $p=0.0005$; Control N=44 myofibers; si Arpc5 N=41
590 myofibers. Results are from three independent experiments. (**J**) To assess the impact of Arpc5
591 in EC-coupling, in vitro myofibers differentiated for 7-8 days expressing GCaMP are stimulated
592 with 10 V at a frequency of 0.5 Hz to elicit membrane depolarization which ultimately results in
593 calcium release and cell contraction. (**K**) Subcellular GCaMP fluorescence kymographs from 8
594 different myofibers of control (Scramble) or Arpc5 (siArpc5) are shown. Orange marks indicate
595 electrical pulses. (**L**) Quantification of the percentage of myofibers from **K** with GCaMP
596 fluorescence transients synchronised with the electrical pulse. Control N=40, si Arpc5 N=62.
597 Results are from three independent experiments. (**M**) Representative contraction tracing
598 recordings from control (Scramble) or Arpc5 (si Arpc5) depleted myofiber. Orange marks indicate
599 electrical pulses. (**N**) Quantification of the percentage of contracting myofibers from **M**. Control
600 N=43, siArpc5 N=36. Results are from three independent experiments. (**O**) Quantification of the
601 percentage of myofibers from **M** that contract in synchrony with the electrical impulse. Control
602 N=41, siArpc5 N=35. Results are from three independent experiments. Blue lines on all plots
603 represent mean values. Black lines in all plots represent the standard error of the mean (SEM).

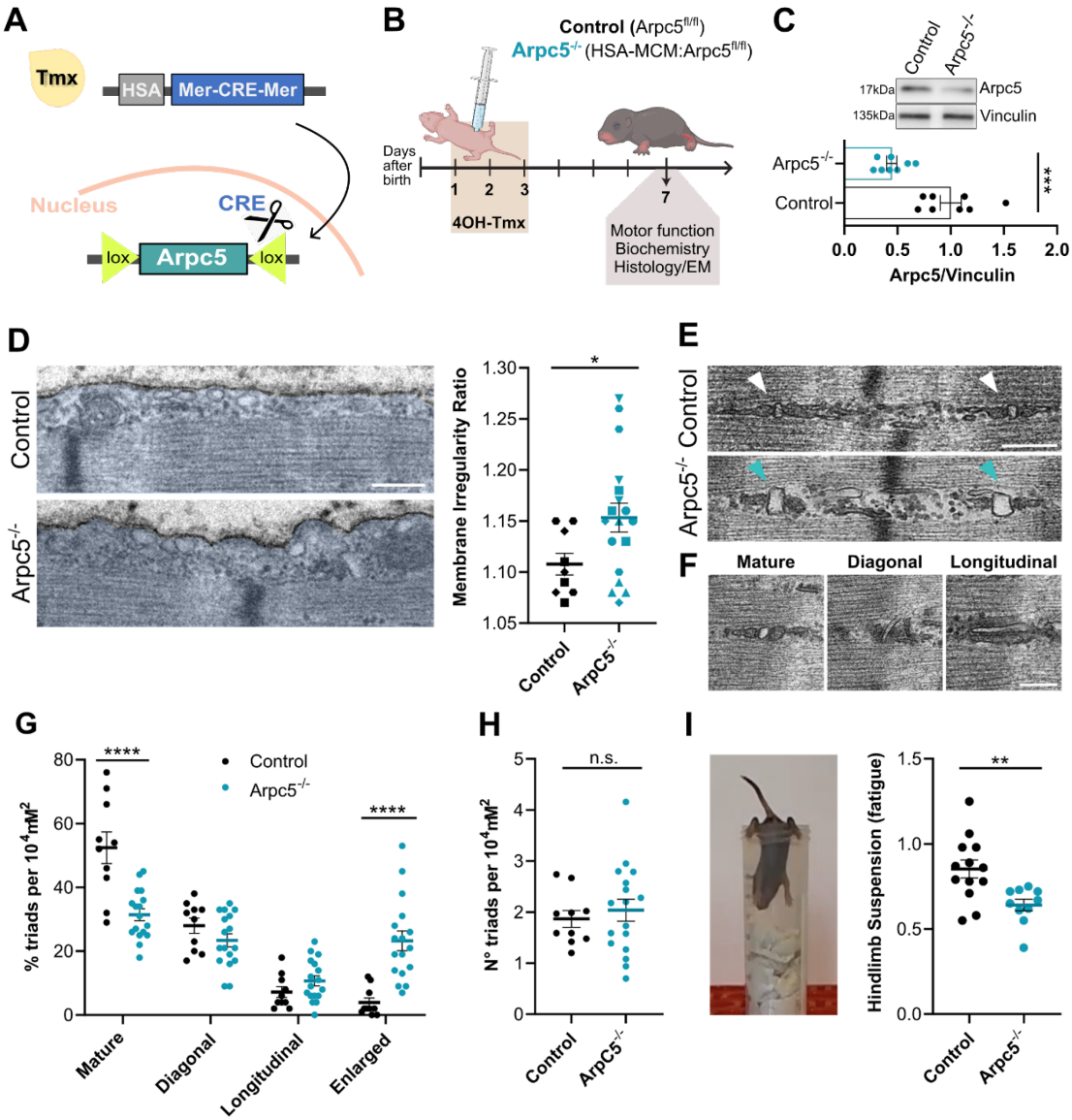

604

605 **Fig. 4 - Postnatal depletion of Arpc5 compromises triad structure and muscle function.** (**A**)
606 Schematic of the Cre-lox knockout strategy to induce skeletal-muscle specific depletion of Arpc5.
607 (**B**) Schematic of the inducible skeletal-muscle specific HSA-MCM mouse model used in this
608 study. Daily 4OH-tamoxifen administration from P1 to P3 was used to induce skeletal muscle-
609 specific Arpc5 depletion. At P7, locomotion was evaluated and the hindlimb posterior muscles
610 were collected for TEM analysis. (**C**) Upper panel, representative Western blots showing Arpc5
611 and Vinculin levels in skeletal muscle of P7 Control and Arpc5$^{-/-}$ mice. Lower panel, quantification
612 of Western blots, showing a significant decrease of Arpc5 protein levels in Arpc5$^{-/-}$ mice. The band
613 intensity of each protein was normalized against vinculin, and the results are shown as fold vs
614 the average of littermate controls. Statistic: unpaired 2-tailed Student's t test, with Mann-Whitney
615 test, p=0.0002. (**D**) Left panel, TEM representative images of longitudinal hindlimb muscle from
616 control (Control) or Arpc5$^{-/-}$ mice. The myofiber cytoplasm is pseudocolored in light blue. Note the
617 darker contour line outlining the myofiber plasma membrane. Scale bar 500 nm. Right panel,
618 quantification of membrane irregularity ratio in myofibers from P7 Control and Arpc5$^{-/-}$ mice,
619 measuring the deviation of a surface from a straight line. Values higher than 1 indicate a rougher
620 membrane. Statistic: unpaired 2-tailed Student's t test, with Welch's correction, p=0.0157. (**E**)
621 TEM representative images of myofibers from control (Control) or Arpc5$^{-/-}$ mice. White
622 arrowheads indicate mature triads (one transverse elongated t-tubule in contact with two adjacent
623 ER compartments). Green arrows indicate enlarged t-tubules, forming an abnormal triad. Scale
624 bar 250 nm. (**F**) Representative images of triads with t-tubule and ER with various morphologies

- longitudinal, diagonal, and mature - indicated by white arrow and reflecting progressive changes in postnatal triad maturation. Scale bar 200 nm. (**G**) Quantifications of the percentage of diagonal, longitudinal, mature and enlarged triads normalized for cell area (10^4 μm^2) in myofibers from P7 Control and Arpc5$^{-/-}$ mice. Statistic: 2-way ANOVA, Sidack's multiple comparisons test; adjusted p value mature normal/enlarged triads <0.0001. (**H**) Quantifications of the number of all mature triads normalized for cell area (10^4 μm^2). Statistic: unpaired 2-tailed Student's t test, non-parametric Mann–Whitney test was used, p>0.05. (**I**) Quantification of the fatigue shown by P7 Control and Arpc5$^{-/-}$ neonates while performing the hindlimb suspension test. Fatigue was assessed by calculating the ratio between the time to fall in the final and initial measurements during the hindlimb suspension test. A lower fatigue value indicates greater fatigue in the mouse. Control N=13 Arpc5$^{-/-}$ N=10 mice. Statistic: unpaired 2-tailed Student's t test, with Welch's correction, p=0.0032. Black horizontal lines in all plots represent mean values. Black vertical lines in all graphs represent SEM.

638 ## Materials and Methods

639 ### T-tubule labelling in mature myofibers

640 All procedures using animals were approved by the Institutional Ethics Committee and
641 followed the guidelines of the Portuguese National Research Council Guide (DGAV). Ex
642 vivo isolated single myofibers from Extensor Digitorum Longus (EDL) muscles were
643 generated using the protocol previously described (*34*). EDL muscle was explanted from
644 8- to 12-week-old male or female C57BL/6J mice and then digested in Dulbecco's
645 modified Eagle's medium (DMEM, Invitrogen) containing 0.2% (w/v) type I collagenase
646 (Sigma) for 2 h at 37°C. Mechanical dissociation of fibers was performed using a thin
647 Pasteur pipette in a transilluminating-fluorescent stereomicroscope. Single fibers were
648 collected and plated in ibidi-35mm-dishes pre-coated with 1% (v/v) matrigel in Iscove's
649 Modified Dulbecco's Media (IMDM, Invitrogen) with Glutamax. After plating, cells were
650 covered with an upper coating of ice-cold 50% (v/v) matrigel coating in IMDM with
651 Glutamax. Plated myofibers were maintained in 10% (v/v) horse serum (Fisher Scientific)
652 plus IMDM with Glutamax for the duration of the experiment. To visualize t-tubule
653 dynamics, plated myofibers were labelled for 30 min with CellMask Orange (1 μM,
654 Invitrogen).

655

656 ### In vitro myofibers

657 All animal procedures were approved by the institutional ethics committee and followed
658 the guidelines of the National Research Council Guide for the care and use of laboratory
659 animals. In vitro myofibers were differentiated as previously described (*44*) from primary
660 myoblasts isolated from 5 to 7-day-old mixed-gender C57BL/6 mice. Tibialis anterior
661 (TA), EDL, gastrocnemius and quadriceps muscles were dissected and kept in ice-cold
662 PBS. Muscles were digested mechanically using surgical scissors and incubated for 90
663 min at 37ºC with agitation in collagenase type V (Sigma) and dispase II (Roche) in DPBS.
664 Digestion was stopped by mixing 10% (v/v) of fetal bovine serum (FBS) plus 1% (v/v) of
665 Penicillin-Streptomycin IMDM with Glutamax. The cells suspension was centrifuged for
666 5 min at 75 x g to remove debris followed by a second centrifugation for 5 min at 350 x
667 g. After centrifugation, cells were resuspended in the same medium and pre-plated for 4
668 hours to allow for fibroblasts adherence. The cells remaining in suspension were
669 collected, centrifuged for 5 min at 350 x g and plated at a density of 220 000 cells/ml in
670 20% (v/v) FBS plus IMDM with Glutamax in ibidi 35 mm dishes pre-coated with 1% (v/v)
671 matrigel in IMDM with Glutamax. After three days of proliferation, medium was replaced

672 by 10% (v/v) horse serum IMDM with Glutamax supplemented with 100 ng/ml
673 recombinant agrin to induce differentiation. An ice-cold upper coating of 50% (v/v)
674 matrigel in 10% (v/v) horse serum IMDM with Glutamax was added the following day and
675 fresh medium was added. Experiments were performed either at 4-5 or 7-8 days after
676 differentiation.

677

678 **Mice**

679 Skeletal muscle-specific Arp2/3 knockout mice strains mice were developed by breeding
680 Arpc5 floxed mice (*37*) with mice expressing Cre recombinase (MerCreMer or MCM)
681 double fusion protein under the human α-skeletal actin (HSA) promoter (*38*). The HSA
682 promoter drives the expression of a tamoxifen (TMX)-inducible specifically in skeletal
683 muscle. Upon tamoxifen administration, the Cre recombinase will be translocated in the
684 nucleus where it will excise the Arpc5 floxed gene only in myofibers (Fig. 4A). For each
685 experiment, cre-negative littermates were used as controls ($Arpc5^{WT}$). Both males and
686 females were used without distinction. 4-Hydroxytamoxifen (Sigma, H6278) was injected
687 intraperitoneally (40 µl of 1,3 mg/mL solution) at postnatal (P) days 1, 2 and 3. At P7-P8,
688 motor function was evaluated and/or animals were euthanized by decapitation. Hindlimb
689 muscle was dissected for histological analysis and electron microscopy processing. All
690 the procedures were approved by the Institutional ethics committee and followed the
691 guidelines of the Portuguese National Research Council Guide (DGAV Project Licenses
692 nº 022871/2016 and 004560/2022) for the care and use of laboratory animals.

693

694 **Motor function evaluation**

695 To evaluate motor function postnatally we used a test appropriate to neonates, namely
696 the hindlimb suspension test (*45*). Hindlimb suspension test; pups were placed gently
697 facing down into a 50 mL conical tube, with their hind legs hung over the rim. This was
698 repeated 3 times, with approximately 30 s of resting time among each trial. Finally,
699 fatigue was assessed by calculating the ratio between the time to fall in the final trial and
700 the initial trial. This fatigue index (final time / initial time) reflects the decline in endurance
701 capacity over repeated tests. A lower value indicates a greater degree of fatigue, as a
702 reduced ability to sustain suspension over time.

703

704 **siRNAs, plasmids, and transfections**

705 To image F-actin, GFP-Bin1 myoblasts were transfected with 1 µg plasmid/ibidi-35mm-
706 dish of LifeAct-mCherry (*46*) or mScarlet-I-UtrCH (gift from Dorus Gadella, Addgene
707 plasmid #98823; http://n2t.net/addgene:98823; RRID:Addgene_98823 (*47*)) one day
708 after plating, using Lipofectamine 2000 (Thermo), according to manufacturer's protocol.
709 For Arpc5 depletion, GFP-Bin1 myoblasts at 30% confluency were transfected with
710 Thermo Fisher Silencer Select siRNAs for Arpc5. Two different siRNAs for Arpc5 were
711 used: #1 (ID#s85623) and #2 (ID#s85621) at 20nM/ibidi-35mm-dish using Lipofectamine
712 RNAiMAX (Thermo). Silencer® Select Scramble (ID #4390843) was used as a negative
713 control. Cells were imaged by vtiSIM microscope on the next day (see below).

714 Triadin-GFP (Trisk95-GFP, (*48*), WT-Ezrin (Ezrin-GFP, gift from Guillaume Charras lab)
715 or CA-Ezrin (EzrinT567D-GFP, gift from Guillaume Charras lab) plasmids were
716 transfected to in vitro myofibers three days after plating (differentiation day 0) with 1 µg
717 of DNA per ibidi-35mm-dish of the appropriate plasmid using Lipofectamine 2000
718 (Thermo), according to manufacturer's protocol. To deplete Arpc5 in myofibers, Thermo
719 Fisher Silencer Select siRNAs for Arpc5 #1 (ID#s85623) was transfected 3 days after
720 plating at 20nM/ibidi-35mm-dish using Lipofectamine RNAiMAX (Thermo). Silencer
721 Select Scramble (ID #4390843) was used as a negative control.

722

723 **Generating the GFP-Bin1 myoblast stable cell line**

724 GFP-Bin1 stable cell line of C2C12 myoblasts (GFP-Bin1 myoblasts) was generated
725 using a pLVX-puromycin vector containing Bin1 isoform 8. The lentiviral vector was
726 constructed with VectorBuilder. The vector ID is VB220728-1365nbr, which can be used
727 to retrieve detailed information about the vector on vectorbuilder.com. Lentivirus were
728 produced in HEK 293T cells. To generate stable cell lines expressing exogenous GFP-
729 Bin1, C2C12 myoblasts were plated in a 6-well plate. The cells with a 10% confluency
730 were carefully covered with 0.5 mL of filtered medium containing the lentiviruses and 0.5
731 mL of complete medium was added to myoblasts (1 mL total volume). The medium
732 containing lentiviruses was left over day, then 1 mL of complete fresh medium was
733 added. Cells were allowed to grow until 80% of confluency. Subsequently, the sorted
734 myoblasts were allowed to expand, and the process was repeated for three rounds of
735 sorting to achieve a homogeneous cell population.

736 GFP-Bin1 myoblasts were cultured in DMEM with glutamine (Gibco) supplemented with
737 10% FBS (Gibco) and penicillin-streptomycin (100 U/mL:100 µg/mL; Gibco), at 37°C
738 under 5% CO_2.

739

740 **AAV1-CAG-CAAX-GFP production**

741 The AAV1-CAG-GFP-CAAX was generated following the protocols from Addgene with
742 minor modifications (*49*, *50*). Briefly, production began by triple transfecting the pAAV-
743 CAG-CAAX plasmid (see Supplementary Text for plasmid map) with AAV packaging
744 plasmid expressing Rep2 and Cap1 (#112862, Addgene) and pHelper into 15-cm plates
745 of confluent HEK-293T cells using polyethylenimine (Polysciences Inc., catalog # 23966-
746 100). The cells were harvested three days post-transfection. The purification step was
747 performed by iodixanol gradient ultracentrifugation and the viral fraction concentrated to
748 approximately 150 µL using an Amicon Ultra-15 centrifugal filter unit (Merck, catalog
749 #UFC910024). For measuring virus titer, we performed qPCR (Biorad CFX96 Real-Time
750 PCR system), using primers against Woodchuck Hepatitis Virus Posttranscriptional
751 Regulatory Element (wpre).

752

753 **Fluorescence microscopy**

754 Airyscan images were acquired using a Zeiss LSM980 Airyscan2 microscope, equipped
755 with a 63x Plan-Apochromat DIC oil objective (NA 1.4), unless stated otherwise. Imaging
756 of fixed cells was performed at RT, and imaging of live cells was performed at 37°C with
757 5% of CO_2 using the ZEN 3.8 blue edition. To measure t-tubule growth, images were
758 recorded every 3 sec. Airyscan reconstruction was performed using automatic filter
759 settings. To visualize the t-tubule network of in vitro differentiated myofibers at higher
760 resolution, Airyscan images were processed using joint-deconvolution (jDCV) in ZEN
761 blue, which is an accelerated joint Richardson-Lucy algorithm (Zeiss).

762 For instant structured illumination microscopy (iSIM) imaging, the vtiSIM module
763 (Visitech) equipped on a Nikon Tie microscope with a 100x AC Oil CFI SR HP Apo TIRF
764 objective, and a Photometrics Prime BSI Express Scientific sCMOS camera was used.
765 Timelapse imaging was performed at 37°C with 5% CO_2.

766 To visualize t-tubule dynamics in developing myofibers, the membrane lipid dye
767 CellMask Orange (1 µM, Invitrogen) was added to 4 days differentiated myofibers 5-10

768 min before imaging. T-tubule and/or Triadin-GFP dynamics were recorded by timelapse
769 imaging using Airyscan microscopy (see above).

770 To visualize actin dynamics near growing t-tubules, GFP-Bin1 myoblasts transfected
771 with LifeAct-mCherry or mScarlet-I-UtrCH were imaged by vtiSIM timelapse every sec
772 for 3 min.

773 To visualize t-tubule network and t-tubule clusters, developed in vitro myofibers
774 (differentiation day 7) were incubated with 1 µM CellMask Deep red (Invitrogen).
775 Spinning disk confocal imaging was performed using a Zeiss Axio Observer microscope
776 equipped with a Yokogawa CSU-X1 scanning unit, an Evolve 512 EMCCD camera and
777 a 63x Plan-Apochromat DIC oil objective (N.A. 1.4), using the ZEN 3.2 blue edition
778 software. Cells were kept at 37°C and 5% CO_2. Myofibers with more than three t-tubule
779 clusters were visually quantified using Fiji software (*51*) and the percentage of cells with
780 t-tubule clusters was plotted using GraphPad.

781

782 **Drug treatments**

783 Cells were treated with 100 µM of CK666 (Sigma) for Arp2/3 inhibition. A final
784 concentration of 125 µM of para-aminoblebbistatin (Motorpharma) was used to block
785 myosin-II. To inhibit Ezrin phosphorylation, NSC668394 (MedChemExpress) was used
786 at 50 µM. The number of growing tubules or t-tubules was assessed immediately after
787 drug treatments for GFP-Bin1 myoblasts and after 5 min for myofibers. T-tubule and
788 tubule dynamics were recorded by timelapse imaging using Airyscan microscopy. GFP-
789 Bin1 myoblasts treated with para-aminoblebbistatin or glycerol were recorded by
790 timelapse imaging using vtiSIM microscopy.

791

792 **Glycerol treatment**

793 Myoblasts and developing myofibers were exposed to 225 mM and 45 mM of glycerol,
794 respectively, to induce hyperosmotic shock. The number of growing t-tubules was
795 performed 3 min after glycerol treatment for GFP-Bin1 myoblasts and after 5 min for
796 myofibers. Myofiber t-tubule dynamics were recorded by timelapse imaging using
797 Airyscan microscopy. GFP-Bin1 myoblasts t-tubule dynamics were recorded by
798 timelapse imaging using vtiSIM microscopy.

799

800

801

802 **Immunostainings**

803 Developing myofibers (differentiation day 4) or differentiated myofibers (differentiation
804 day 7) were fixed in 4% paraformaldehyde in PBS for 10 min at room temperature and
805 permeabilized with 0.5% Triton X-100 for 5 min. Cells were blocked in a solution
806 containing 10% goat serum, 5% BSA and VisUBlock Mouse on Mouse Blocking Reagent
807 (R&D Systems, VB001). Primary and secondary antibodies were diluted in 0.1%
808 saponin. Cells were incubated with primary antibodies overnight at 4°C and washed
809 three times for 10 min with PBS. Cells were incubated with secondary antibodies for 1 h
810 at room temperature and washed three times for 10 min with PBS. Cells were mounted
811 with Fluoromount-G (Invitrogen).

812

813 **Junctophilin1 immunostaining**

814 For Junctophilin1 immunostaining in differentiated myofibers (day 7), we used an anti-
815 JPH1 antibody (1:200 dilution, Invitrogen, 40-5100) and an anti-rabbit Alexa Fluor 488
816 secondary antibody (1:400, Life Technologies). Phalloidin conjugated with an Alexa
817 Fluor 647 (1:200, Life Technologies) was used to stain filamentous actin. Myofibers were
818 imaged using the vtiSIM microscope (VisiTech).

819

820 **p-ERM and NM-myo2B localization at the plasma membrane**

821 To label the plasma membrane, in vitro primary myofibers were infected on day 2 of
822 differentiation with the AAV1-CAG-GFP-CAAX (1.535 x 10^^{7} genome copies to a 35mm
823 dish containing myofibers at approximately 70-80% confluency). The virus was washed
824 on the next day, with differentiation media containing 1 µg/ml of agrin. At day 4 of
825 differentiation, cells were fixed and stained as described above.

826 To label pERM we used an anti-Phospho-Ezrin (Thr567)/Radixin (Thr564)/Moesin
827 (Thr558) (1:200 dilution, Cell Signaling Technology #3141) and anti-rabbit Alexa Fluor
828 555 secondary antibody (1:400, Life Technologies). To label NM-myo2B, cells were
829 incubated with an anti-Non-muscle Myosin Heavy Chain II-B (NM-myo2B) antibody
830 (1:200 dilution, Biolegend) and anti-rabbit Alexa Fluor 555 secondary antibody (1:400,
831 Life Technologies). Cells were also co-stained with an anti-GFP antibody (1:200 dilution,
832 Roche #11814460001) and anti-mouse Alexa Fluor 488 secondary antibody (1:400, Life
833 Technologies). Cells were imaged by Airyscan using the LSM980 microscope with a 40x
834 LD C-Apochromat, N.A. 1.1, Water immersion objective.

835 To quantify the number of foci of NM-myo2B, using Fiji, we drew rectangle ROIs with a
836 constant width of 0.8 µm along the CAAX-GFP channel. The NM-Myo2B fluorescence

intensity signal over that ROI was then plotted and the number of peaks (corresponding to NM-Myo2B foci) was measured with the Find Peaks BAR tool (*52*) using a mean amplitude of 100. The number of peaks in each ROI was divided by the respective area of the ROI, and these values were plotted as the number of NM-Myo2B foci per ROI area (μm^2).

To quantify pERM at the plasma membrane, we used the CAAX-GFP signal to identify the plasma membrane and drew a line of 10 µm length by 10 pixels width on top of the signal, and extracted the single-pixel intensity values of pERM. To calculate the pERM intensity signal, we averaged the single-pixel intensity over the 10 µm line. To measure the pERM coefficient of variation, we calculated the standard deviation of the single-pixel intensity over the 10 µm line divided by the mean of fluorescence.

Atomic force microscopy

Atomic force microscopy (AFM) imaging of developing myofibers was performed using a NanoWizard IV system (Bruker-JPK Instruments, Berlin, Germany) mounted atop an Axiovert 200 inverted optical microscope (Carl Zeiss, Jena, Germany). To avoid cell contraction during acquisition, developing myofibers (differentiated for 4 days) were imaged in Tyrode Buffer (140 mM NaCl, 5 mM KCl, 2 mM $MgCl_2$ and 10 mM HEPES, pH 7.2). For AFM imaging, oxidized and sharpened silicon probes with a nominal tip radius of approximately 6 nm, a resonance frequency of 60 kHz, and a spring constant of 3 N/m were employed. Scanning was performed at an optimized speed of 0.3 Hz using a minimal applied force to avoid damaging the sample. Images were acquired at a resolution of 512 × 512 pixels.

Surface roughness measurements were conducted on live cells following four days of differentiation, using the same equipment. Experiments were performed at 25°C in Tyrode's solution, employing the Quantitative Imaging (QI) mode to capture height data. Non-functionalized qp-BioAC CB2 cantilevers (Nanosensors, Neuchâtel, Switzerland) with partial gold coating and quartz-like tips, featuring a nominal spring constant of 100 pN/nm, were used. Differential interference contrast (DIC) microscopy facilitated accurate positioning of the cantilever tip over both Arpc5 KD and scramble control cells. QI-mode height maps of 5 µm × 5 µm were acquired with a vertical (z) range of 2 µm. Images were recorded at a resolution of 256 × 256 pixels with a pixel dwell time of 20 ms. During each approach, the cantilever-to-cell distance was dynamically adjusted to maintain a maximal applied force of 1 nN prior to tip retraction. For each experimental condition, a minimum of 12 height images were obtained, with all samples analyzed in triplicate. Image processing was performed using JPK Image Processing software (v.

873 8.0.144) to calculate average roughness (Ra) and root mean square roughness (Rq).
874 For each height map, roughness was determined in five distinct 0.5 µm × 0.5 µm square
875 regions located between Z-bands. In total, surface topographies of 12 control cells and
876 15 Arpc5 KD cells were analyzed.
877
878 **Image analysis**
879 All images were processed in Fiji (*51*). For cell drift correction we used the Fiji plugin
880 Fast4Dreg (*53*).

881 For t-tubule growth speed measurements, manual tracking of the tip of the t-tubule during
882 the timelapse was performed using Fiji manual tracking.

883 The number of growing t-tubules was manually recorded using the Fiji cell counter tool.
884 This value was then normalized for the cell area. All quantifications were performed
885 within 2 min timelapses (42 frames). For the cells expressing WT-Ezrin or CA-Ezrin, the
886 number of growing t-tubules was measured in cells containing GFP positive signal only.

887 To measure Triadin-GFP mean speed in developing myofibers, we used Airyscan
888 images of Triadin-GFP timelapses acquired every 3 sec for 2 min. Since Triadin-GFP
889 localizes as distinct spots, we used the Fiji plugin Trackmate (*54*) to track Triadin-GFP
890 spots over time in myofibers. To detect Triadin-GFP spots we used the LoG detector
891 with an estimated object diameter of 0.5 µm and a quality threshold of 5, 10 or 20. We
892 then linked the spots to generate tracks, by using the LAP tracker with a max distance
893 of 0.5 µm and no gap closing. To have enough datapoints to calculate speed trajectories,
894 we only considered tracks that lasted more than 10 frames (30 sec). The resulting
895 tracked Triadin-GFP spots were then used to calculate mean speed.

896 To quantify actin dynamics in the vicinity of growing t-tubules, we manually selected a
897 ROI around GFP-Bin1 growing tubules (as the ones represented in fig. S2A and S2C),
898 including a few timepoints before the GFP-Bin1 signal was observed using Fiji software.
899 We then extracted at each timepoint the average of fluorescence intensity per μm^2 for
900 GFP-Bin1, LifeAct-mcherry or mScarlet-I-UtrCH using the Fiji software. Values were
901 normalized for the initial corresponding average intensity, and these normalized intensity
902 values per μm^2 over time were plotted using GraphPad.

903 To automatically count the number of Junctophilin 1 (JPH1) puncta, a maximum
904 projection of the Z-stack images that were in focus was first performed using Fiji. Then,
905 a rectangular ROI with an area of 175.552 μm^2 was drawn along the myofiber length. To
906 detect the puncta automatically, we used the LoG detector tool from the Fiji TrackMate

907 plugin (*54*). LoG filters for puncta detection were a blob diameter of 0.5 µm and an
908 intensity threshold of 5. To analyse the number of JPH1 puncta per μm^2, the number of
909 detected puncta was normalized for ROI area and plotted.

910

911 **Western blot**

912 Cell extracts were collected in 100 mM Tris-HCl pH 8 with 1% (w/v) SDS. Tissue was
913 extracted from snap-frozen muscle samples and homogenized using an Omni Soft
914 Tissue Tip Homogenizer (Biolabproducts GmbH). Protein lysates were prepared using
915 RIPA buffer (NaCl 150 mM, EDTA 5 mM, 1% (v/v) Triton X-100, 0.5% (v/v) NP-40, Tris
916 50 nM pH 7.5) with protease and phosphatase inhibitors (Roche). All protein
917 quantification was performed using the BCA Protein Assay Kit (Pierce) following the
918 manufacturer's protocol. Samples were denatured in Laemmli buffer and heated at 95°C
919 for 5 min. 10-30 ug of total protein was loaded onto a 10% (v/v) precast polyacrylamide
920 gel (Bio-Rad) and transferred to a nitrocellulose membrane for 75 min at 100 V. The
921 membranes were blocked with Tris-buffered saline with 0.1% (v/v) Tween 20 (TBS-T)
922 containing 5% skim milk, followed by incubation with primary antibodies, overnight at
923 4°C. Membranes were washed and incubated with HRP-conjugated secondary
924 antibodies for 1 hour at room temperature and washed three times before image
925 acquisition. Images were acquired using Amersham ImageQuant800 (Cytiva).
926 Antibodies used were: anti-Arpc5 (1:500 Santa Cruz Biotechnology, sc-166760); anti-
927 Vinculin (1:1000, Sigma, V9131); anti-rabbit HRP (1:5000, Thermo Scientific) and anti-
928 mouse HRP (1:5000, Thermo Scientific).

929

930 **Cryo-ET sample preparation**

931 GFP-Bin1 myoblasts were grown to approximately 60% confluency and then diluted to
932 a confluency of 10%. EM grids (Quantifoil R3.5/1 Au 200 mesh) were glow-discharged
933 using a plasma cleaner (PLASMAFLO PDC-FMG-2, Harrick Plasma) and then placed in
934 a 35mm MatTek dish in a flow hood. 300 µL of 5 µg/mL Fibronectin (Sigma-Aldrich,
935 341635) was added to the dish, covering the EM grids. The dish with the grids inside
936 was then sterilized under UV light for 1.5 h. After simultaneous coating and sterilization,
937 fibronectin was removed from the MatTek dish. The grids were then washed twice with
938 PBS and stored in approximately 300 µl of medium (DMEM high glucose+pyruvate+L-
939 glutamine; 10% (v/v) FBS + 1% (v/v) PenStrep).

940 Once the cells were ready, the medium in the grid-containing dish was removed, and
941 diluted cells were added to the dish. The cells were seeded on the EM grids at 37ºC 5%
942 CO_2 overnight (~15 h). The following day, grids were inspected under an inverted
943 biological microscope (Medline Scientific, 3650.0000) to check the cell density and
944 ensure grid integrity. Grids with minimally broken areas and well-distributed cells were
945 plunge frozen using Leica GP2 with back blotting for 15 s and an additional movement
946 of 0.5 mm at 37ºC and 90% humidity.

947

948 **Correlative light and electron microscopy**

949 Frozen grids were first loaded onto a Titan Krios microscope (Thermo Fisher) operated
950 at an accelerating voltage of 300 kV with a K3 detector and a BioQuantum energy filter
951 (Gatan). Grid atlas images were collected to check the ice quality and the cell density
952 using EPU software (Thermo Fisher). After locating the spread cells, grids were
953 transferred onto a cryo-light microscope (Leica THUNDER Imager EM Cryo CLEM). Z
954 stack fluorescence and bright field images were taken of the located spread cells using
955 LAS X software at 50x magnification. With the fluorescence images processed using
956 THUNDER technology, individual tubular fluorescence signals were observed. The
957 fluorescence images were saved for fluorescence microscopy (FM) and electron
958 microscopy (EM) image correlation. The grids were then transferred back to a Titan Krios
959 microscope (Thermo Fisher) operated at an accelerating voltage of 300 kV, with Selectris
960 X image filter (Thermo Fisher) and Falcon 4i camera (Thermo Fisher). Medium
961 magnification atlases were taken and combined on each fluorescence-labelled cell for
962 manual correlation and locating the regions of interest. Empty holes and dark features
963 were used as markers to facilitate the manual correlation (fig. S3B and S3C). After
964 correlation, ROI with fluorescence signals were targeted for cryo-ET tilt series data
965 collection. 114 tilt series were collected using TOMO5 software with a dose symmetric
966 tilt scheme +/- 60° with the step size of 3° at the magnification of ×42,000, pixel size of
967 3.0 Å, dose rate of 12.6 e^-/pixel/s, exposure time of 2.69s and total dose per micrograph
968 of 3.66 e^-/ $Å^2$.

969

970 **Tomogram reconstruction**

971 Tomograms were reconstructed using RELION 4.1 tomography pipeline (*55*). Raw data
972 were imported into RELION followed by motion correction with RELION's own

implementation of MotionCor2 (*56*) and CTF correction with ctffind 4.1 (*57*). Tilt images with significant contamination and grid bars were manually excluded from further data processing in a Napari-based viewer (Exclude Tilt Images job). Then each tilt series was aligned using IMOD [CM4] patch tracking with Patch size 100 nm and Patch overlap 50%. The aligned tilt series were used to generate tomograms with a binned pixel size of 10 Å. Tomograms were denoised using CryoCARE to improve the signal-to-noise level (*58*). CryoCARE training was performed with 1200 sub-volumes per tomogram and a sub-volume dimension of 72 pixel. Upon inspecting the tomograms, we found that 58 contained vesicular as opposed to tubular membrane structures (as shown in fig. S3G) and were excluded. 23 of the tomograms were discarded due to the presence by non-vitreous ice and could not be used for segmentation. Additionally, 27 tomograms did not correlate well with fluorescence signals because of the ambiguity of fluorescence and the lack of correlation markers, which posed challenges for manual correlation. 6 tomograms displayed tubular structures at locations where fluorescence was observed. From these, the 3 highest quality tomograms were selected for segmentation and further analysis.

Tomogram segmentation

Tomograms were processed using IsoNet to further improve the signal-to-noise (snr) level (*59*). The following parameters were used: CTD deconvolve snrfalloff of 0.5, mask making density_percentage of 100, std_percentage of 100, and z_crop of 0.17. Then, IsoNet-processed tomograms were cropped to remove regions lacking t-tubule structures to simplify segmentation. Segmentation was performed using the neural network-based software Dragonfly (Dragonfly 2024.1 [Computer software]. Comet Technologies Canada Inc., Montreal, Canada; software available at https://dragonfly.comet.tech/). For each tomogram, actin and membrane structures were manually annotated on 5-12 sub-areas across different slices of the tomogram. The segmented data were then used to train multiple deep-learning models. The model segmenting the highest number of actin filaments on test slices was selected to segment the entire tomogram. The UNet++ model (2.5D, 3 slices, depth level of 5, and initial filter count of 32) was used for tomograms 1 and 2. Additionally, a pretrained UNet model provided by the Dragonfly team (depth level of 5 and initial filter count of 64) was utilized for tomogram 3. The segmentations were manually cleaned and corrected in Dragonfly. The segmented actin and membrane structures were rendered into a 3D contour mesh and smoothed over five to ten iterations for 3D visualization in fig. S3I and fig. S4. Movies

1008 were created by exporting the segmented actin and membrane structures as binary files,
1009 converting these into two MRC files, and then importing them along with a contrast-
1010 inverted 3D tomogram into ChimeraX for visualization (*60*).

1011

1012 **Tomogram analysis**

1013 For tomogram analysis, sub-tomograms proximal to the t-tubules and distant from the t-
1014 tubules were selected. The sub-volumes near t-tubules were constrained to regions no
1015 more than 200 nm from the t-tubule structures. Actin branches – inferred from the relative
1016 position of two connected filaments - within these boxes were identified, labelled, and
1017 counted. For control purposes, sub-volumes located more than 200 nm away from t-
1018 tubules were also identified, and suspected actin branches within these control sub-
1019 volumes were similarly labelled and counted. In total, 7 sub-volumes were selected to
1020 determine the number of actin branches near the t-tubules, and 3 sub-volumes were
1021 selected as controls.

1022

1023 **Single-myofiber contraction and calcium transient assays**

1024 In vitro myofibers were plated on 35mm fluorodishes (World Precision Instruments). After
1025 7-8 days of differentiation, developed myofibers were imaged using a Nikon Eclipse Ti
1026 microscope. Myofibers were kept at 37°C and CO_2 5% using an Okolab stage incubator
1027 throughout all experimental procedures. Electrical field stimulation using the MyoPacer
1028 system (Ionoptix) was used to induce excitation-contraction of myofibers using 10 V at
1029 0.5 Hz frequency pulses with a duration of 20 ms.

1030 To measure cytosolic calcium transients during electrical pulses, myofibers at
1031 differentiation day 3-4 were infected using 1 µl/mL of the AAV9-
1032 pAAV.CAG.GCaMP6s.WPRE.SV40 (Addgene viral prep # 100844-AAV9; the plasmid
1033 was a gift from Douglas Kim & GENIE Project (*61*)). After overnight incubation, the media
1034 was replaced with differentiation media (IMDM with Glutamax supplemented with 100
1035 ng/mL recombinant agrin). After 7-8 days of differentiation, GCaMP fluorescence during
1036 electrical field stimulation was recorded using a 60x Plan Apo DM Ph3 (NA 1.4) objective,
1037 and an Andor Sona CSC-00324 camera at a 20 ms frame rate with the NIS-Elements
1038 AR 5.42.05 software. Fiji software was then used to generate subcellular GCaMP
1039 fluorescence kymographs by drawing a 475.7 μm^2 square ROI along the myofiber that
1040 was then was maximum projected, generating GCaMP fluorescence kymographs. The

1041 number of cells that presented GCaMP transients synchronous with the electrical pulse
1042 was then quantified from these kymographs, and plotted.

1043 For single-myofiber contraction tracing, electrical field stimulation was performed as
1044 mentioned above. Individual cell contractions were recorded with a MyoCam-S3 camera
1045 (Ionoptix) and a 40x CFI Plan Apochromat Lambda D objective (NA 0.95), using the
1046 IonWizard 7.7.3.180 software. Contraction kinetics were based on CytoMotion (Ionoptix)
1047 Pixel Correlation changes relative to the reference frame taken at rest (i.e. before
1048 electrical pulses). To generate single-myofiber contraction tracings, pixel correlation
1049 (a.u.) curves were plotted using the Cytosolver Cloud (Ionoptix). Myofibers that during
1050 the electrical stimuli did not contract, contract, present synchronous or asynchronous
1051 contraction during the electrical stimulus were then quantified and plotted.

1052

1053 **Transmission electron microscopy**

1054 Developed myofibers (7 days of differentiation) were fixed for 1 h at 4 °C in 0.1 M
1055 Sorensen's Phosphate Buffer pH 7.4 containing 2.5% (v/v) glutaraldehyde (Science
1056 Services EMS), 2% (v/v) formaldehyde (Science Services EMS) and 50 mM calcium
1057 chloride (Sigma). Samples were postfixed for 1 h at 4ºC in the dark with 0.1 M Sorensen's
1058 Phosphate Buffer pH 7.4 containing 1% (w/v) osmium tetroxide (Science Services EMS)
1059 and 0.8% (w/v) potassium ferrocyanide (Sigma-Aldrich). After five washes with distilled
1060 water, samples were stained for 1h at room temperature with 0.5% (w/v) uranyl acetate
1061 (Analar). Dehydration was performed using an ethanol gradient (30% 10 min room
1062 temperature, 50% 10 min room temperature, 75% overnight 4ºC, 90% 10 min room
1063 temperature, and 100% three times 10 min each room temperature). Samples were
1064 embedded in Embed-812 epoxy resin (Science Services EMS) and hardened at 60 °C
1065 for at least 24 h. Ultrathin sections (70 nm) were obtained and collected in homemade
1066 formvar-carbon coated copper-palladium slot grids and counter-stained with 1% (w/v)
1067 uranyl acetate in 70% methanol and Reynolds lead citrate, for 5 min each.

1068

1069 For muscle tissue from mice, longitudinal sections of postnatal myofibers from mouse
1070 neonates were generated from hindlimb muscles. For this, after sacrifice, the skin was
1071 removed and the whole mice leg was incubated with fixative (0.1 M Sorensen's
1072 Phosphate Buffer pH 7.4 containing 2.5% (v/v) glutaraldehyde (Science Services EMS),
1073 2% (v/v) formaldehyde (Science Services EMS) and 50 mM of calcium chloride (Sigma))
1074 for 1 h, to preserve muscle structure. Rinse in 0.1M cacodylate buffer and dissecting by
1075 cutting small longitudinal pieces (<1mm3). These small pieces were incubated overnight

at 4°C with fixative 0.1 M Sorensen's Phosphate Buffer pH 7.4 containing 2.5% (v/v) glutaraldehyde (Science Services EMS), 2% (v/v) formaldehyde (Science Services EMS) and 50 mM calcium chloride (Sigma). Samples were postfixed for 2 h at 4ºC in the dark with 0.1 M Sorensen's Phosphate Buffer pH 7.4 containing 2% (w/v) osmium tetroxide (Science Services EMS) and 0.8% (w/v) potassium ferrocyanide (Sigma-Aldrich). After five washes with distilled water, samples were stained for 1h at room temperature with 0.5% (w/v) uranyl acetate (Analar). Dehydration was performed using an ethanol gradient (30% 10 min room temperature, 50% 10 min room temperature, 75% overnight 4ºC, 90% 10 min room temperature, and 100% three times 10 min each room temperature). Samples were embedded in Embed-812 epoxy resin (Science Services EMS) and hardened at 60 °C for at least 24 hours. Ultrathin sections (70 nm) were obtained and collected in homemade formvar-carbon coated copper-palladium slot grids and counter-stained with 2% (w/v) uranyl acetate in 70% MetOH and Reynolds lead citrate, for 5 min each.

Regions of interest were mapped with SerialEM software and tiles of differentiated cells were acquired using a FEI Tecnai G2 Spirit BioTWIN (120 kV) transmission electron microscope with an Olympus-SIS Veleta CCD Camera.

Stitching was performed using the IMOD blendemont function (*62*). Stitched tiles were opened in Fiji and we counted the number of triads (one t-tubule connected to two ER) in each tile, and normalized it to the cell area. To count t-tubules or measure their area in myofibers, we identified the membrane objects that had a low electron-dense lumen, and that were contacting the ER (green or blue arrowheads in Fig. 3E and white arrowheads in Fig. 4). Area was measured by drawing a region of interest along the t-tubule membrane, using the drawing tool from Fiji software. We quantified membrane irregularity ratio as a measure of surface roughness. The irregularity ratio was calculated by dividing the length of the manually traced membrane contour by the length of a straight horizontal reference line drawn between the two ends of the membrane segment. Membrane outlines were manually traced using high-resolution TEM images in Fiji software. Values equal to one correspond to a flat membrane. Values higher than one correspond to the degree of membrane irregularity/roughness.

1110 **Data representation and statistics**

1111 All graphs were generated and statistical analyses were conducted using GraphPad
1112 Prism v8. Normality testing was carried out using the Shapiro-Wilk test, with an alpha
1113 level=0.05. Details about the tests used are described in the Figure legends.

Supplementary Text

pAAV-CAG-GFP-CAAX_VectorMap

ttgagatccttttttctgcgcgtaatctgctgcttgcaaacaaaaaaaccaccgctaccagcggtggtttgtttgccggatcaagagctac
caactctttttccgaaggtaactggcttcagcagagcgcagataccaaatactgttcttctagtgtagccgtagttaggccaccacttcaa
gaactctgtagcaccgcctacatacctcgctctgctaatcctgttaccagtggctgctgccagtggcgataagtcgtgtcttaccgggttg
gactcaagacgatagttaccggataaggcgcagcggtcgggctgaacggggggttcgtgcacacagcccagcttggagcgaacg
acctacaccgaactgagatacctacagcgtgagctatgagaaagcgccacgcttcccgaagggagaaaggcggacaggtatccg
gtaagcggcagggtcggaacaggagagcgcacgagggagcttccagggggaaacgcctggtatctttatagtcctgtcgggtttcg
ccacctctgacttgagcgtcgatttttgtgatgctcgtcaggggggcggagcctatggaaaaacgccagcaacgcggcctttttacggtt
cctggccttttgctggccttttgctcacatgttctttcctgcgttatcccctgattctgtggataaccgtattaccgcctttgagtgagctgatacc
gctcgccgcagccgaacgaccgagcgcagcgagtcagtgagcgaggaagcggaagagcgcccaatacgcaaaccgcctctcc
ccgcgcgttggccgattcattaatgcagctgcgcgctcgctcgctcactgaggccgcccgggcaaagcccgggcgtcgggcgacctt
tggtcgcccggcctcagtgagcgagcgagcgcgcagagagggagtggccaactccatcactaggggttccttgtagttaatgattaa
cccgccatgctacttatctacgtagccatgctctaggaagatcgtaccattgacgtcaataatgacgtatgttcccatagtaacgccaat
agggactttccattgacgtcaatgggtggactatttacggtaaactgcccacttggcagtacatcaagtgtatcatatgccaagtacgcc
ccctattgacgtcaatgacggtaaatggcccgcctggcattatgcccagtacatgaccttatgggactttcctacttggcagtacatctac
gtattagtcatcgctattaccatggtcgaggtgagccccacgttctgcttcactctccccatctcccccccctccccaccccaattttgtatt
tatttatttttaattattttgtgcagcgatgggggcgggggggggggggcgcgcgccaggcggggcggggcggggcgagggg
cggggcggggcgaggcggagaggtgcggcggcagccaatcagagcggcgcgctccgaaagtttccttttatggcgaggcggcg
gcggcggcggccctataaaaagcgaagcgcgcggcgggcgggagtcgctgcgacgctgccttcgccccgtgccccgctccgccg
ccgcctcgcgccgcccgccccggctctgactgaccgcgttactcccacaggtgagcgggcgggacggcccttctcctccgggctgta
attagcgcttggtttaatgacggcttgtttcttttctgtggctgcgtgaaagccttgaggggctccgggagggccctttgtgcgggggggagc
ggctcggggctgtccgcgggggggacggctgccttcgggggggacggggcagggcggggttcggcttctggcgtgtgaccggcggc
tctagagcctctgctaaccatgttcatgccttcttctttttcctacagctcctgggcaacgtgctggttattgtgctgtctcatcattttggcaaag
aattggatcgggatccccgggtaCCGGTCGCCACCATGGTGAGCAAGGGCGAGGAGCTGTTCACCG
GGGTGGTGCCCATCCTGGTCGAGCTGGACGGCGACGTAAACGGCCACAAGTTCAGCGTG
TCCGGCGAGGGCGAGGGCGATGCCACCTACGGCAAGCTGACCCTGAAGTTCATCTGCAC
CACCGGCAAGCTGCCCGTGCCCTGGCCCACCCTCGTGACCACCCTGACCTACGGCGTGC
AGTGCTTCAGCCGCTACCCCGACCACATGAAGCAGCACGACTTCTTCAAGTCCGCCATGC
CCGAAGGCTACGTCCAGGAGCGCACCATCTTCTTCAAGGACGACGGCAACTACAAGACCC
GCGCCGAGGTGAAGTTCGAGGGCGACACCCTGGTGAACCGCATCGAGCTGAAGGGCATC
GACTTCAAGGAGGACGGCAACATCCTGGGGCACAAGCTGGAGTACAACTACAACAGCCAC
AACGTCTATATCATGGCCGACAAGCAGAAGAACGGCATCAAGGTGAACTTCAAGATCCGC
CACAACATCGAGGACGGCAGCGTGCAGCTCGCCGACCACTACCAGCAGAACACCCCCAT
CGGCGACGGCCCCGTGCTGCTGCCCGACAACCACTACCTGAGCACCCAGTCCGCCCTGA
GCAAAGACCCCAACGAGAAGCGCGATCACATGGTCCTGCTGGAGTTCGTGACCGCCGCC
GGGATCACTCTCGGCATGGACGAGctgtataagggtaaaaagaagaaaaagaagtcaaagacaaagtgtgtaat
tatgtagTGTACAAGTCCGGACTCAGATCTCGAGCTCAagcttatcgataatcaacctctggattacaaaatttgtg
aaagattgactggtattcttaactatgttgctccttttacgctatgtggatacgctgctttaatgcctttgtatcatgctattgcttcccgtatggct
ttcattttctcctccttgtataaatcctggttgctgtctctttatgaggagttgtggcccgttgtcaggcaacgtggcgtggtgtgcactgtgtttg
ctgacgcaacccccactggttggggcattgccaccacctgtcagctcctttccgggactttcgctttccccctccctattgccacggcgga
actcatcgccgcctgccttgcccgctgctggacaggggctcggctgttgggcactgacaattccgtggtgttgtcggggaaatcatcgtc
ctttccttggctgctcgcctgtgttgccacctggattctgcgcgggacgtccttctgctacgtcccttcggccctcaatccagcggaccttcct
tcccgcggcctgctgccggctctgcggcctcttccgcgtcttcgccttcgccctcagacgagtcggatctccctttgggccgcctccccgc
atcgataccgtcgacccgggcggccgcttcgagcagacatgataagatacattgatgagtttggacaaaccacaactagaatgcagt
gaaaaaaatgctttatttgtgaaatttgtgatgctattgctttatttgtaaccattataagctgcaataaacaagttaacaacaacaattgcat
tcattttatgtttcaggttcagggggagatgtgggaggttttttaaagcaagtaaaacctctacaaatgtggtaaaatcgataaggatcttc
ctagagcatggctacgtagataagtagcatggcgggttaatcattaactacaaggaacccctagtgatggagttggccactccctctct
gcgcgctcgctcgctcactgaggccgggcgaccaaaggtcgcccgacgcccgggctttgcccgggcggcctcagtgagcgagcg
agcgcgcagccttaattaacctaattcactggccgtcgttttacaacgtcgtgactgggaaaaccctggcgttacccaacttaatcgcctt
gcagcacatccccctttcgccagctggcgtaatagcgaagaggcccgcaccgatcgcccttcccaacagttgcgcagcctgaatgg
cgaatgggacgcgccctgtagcggcgcattaagcgcggcgggtgtggtggttacgcgcagcgtgaccgctacacttgccagcgccc
tagcgcccgctcctttcgctttcttcccttcctttctcgccacgttcgccggctttccccgtcaagctctaaatcgggggctccctttagggttc
cgatttagtgctttacggcacctcgaccccaaaaaacttgattagggtgatggttcacgtagtgggccatcgccctgatagacggtttttc
gccctttgacgttggagtccacgttctttaatagtggactcttgttccaaactggaacaacactcaaccctatctcggtctattcttttgatttat
aagggattttgccgatttcggcctattggttaaaaaatgagctgatttaacaaaaatttaacgcgaattttaacaaaatattaacgcttaca
atttaggtggcacttttcggggaaatgtgcgcggaacccctatttgtttatttttctaaatacattcaaatatgtatccgctcatgagacaata
accctgataaatgcttcaataatattgaaaaaggaagagtatgagtattcaacatttccgtgtcgcccttattcccttttttgcggcattttgc

1174 cttcctgtttttgctcacccagaaacgctggtgaaagtaaaagatgctgaagatcagttgggtgcacgagtgggttacatcgaactggat
1175 ctcaacagcggtaagatccttgagagttttcgccccgaagaacgttttccaatgatgagcacttttaaagttctgctatgtggcgcggtatt
1176 atcccgtattgacgccgggcaagagcaactcggtcgccgcatacactattctcagaatgacttggttgagtactcaccagtcacagaa
1177 aagcatcttacggatggcatgacagtaagagaattatgcagtgctgccataaccatgagtgataacactgcggccaacttacttctga
1178 caacgatcggaggaccgaaggagctaaccgctttttgcacaacatgggggatcatgtaactcgccttgatcgttgggaaccggagct
1179 gaatgaagccataccaaacgacgagcgtgacaccacgatgcctgtagcaatggcaacaacgttgcgcaaactattaactggcgaa
1180 ctacttactctagcttcccggcaacaattaatagactggatggaggcggataaagttgcaggaccacttctgcgctcggcccttccggct
1181 ggctggtttattgctgataaatctggagccggtgagcgtgggtctcgcggtatcattgcagcactggggccagatggtaagccctcccgt
1182 atcgtagttatctacacgacggggagtcaggcaactatggatgaacgaaatagacagatcgctgagataggtgcctcactgattaag
1183 cattggtaactgtcagaccaagtttactcatatatactttagattgatttaaaacttcatttttaatttaaaaggatctaggtgaagatccttttg
1184 ataatctcatgaccaaaatcccttaacgtgagttttcgttccactgagcgtcagaccccgtagaaaagatcaaaggatcttc
1185

Supplementary Figures

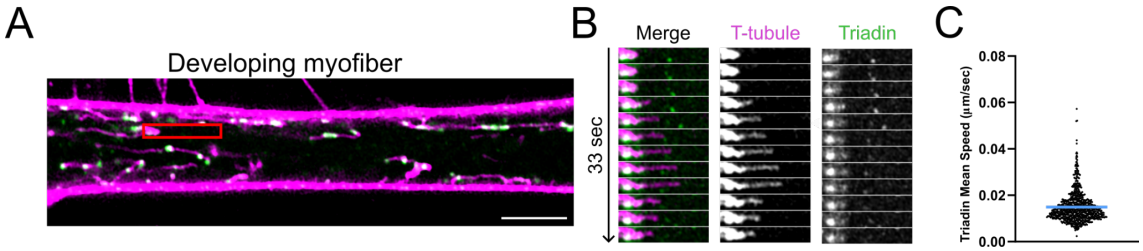

Fig. S1 - T-tubules are dynamic independently of contacts with the ER. Triadin-GFP, an ER transmembrane protein localises at t-tubule - ER contact sites and triads (*63*). (**A**) Timelapse snapshot of an in vitro developing myofiber (differentiation day 4) expressing Triadin-GFP (green), and CellMask DeepRed (magenta) to label t-tubules, was imaged by timelapse every 3 s for 2 min. Scale bar 5 µm. (**B**) Kymograph from red ROI showing that Triadin-GFP is static when t-tubules are growing. In 100% of growing t-tubules, we did not observe Triadin-GFP moving with the t-tubule (N=39 growing t-tubules). (**C**) The plot represents Triadin-GFP mean speed, calculated using trackmate, in five different cells from two independent repeats (N=783 tracks). Triadin-GFP exhibits a negligible average speed of 0.015 µm/s compared to the t-tubule growing average speed of 1.2 µm/s (Fig. 1B). Blue line on plot represents mean value.

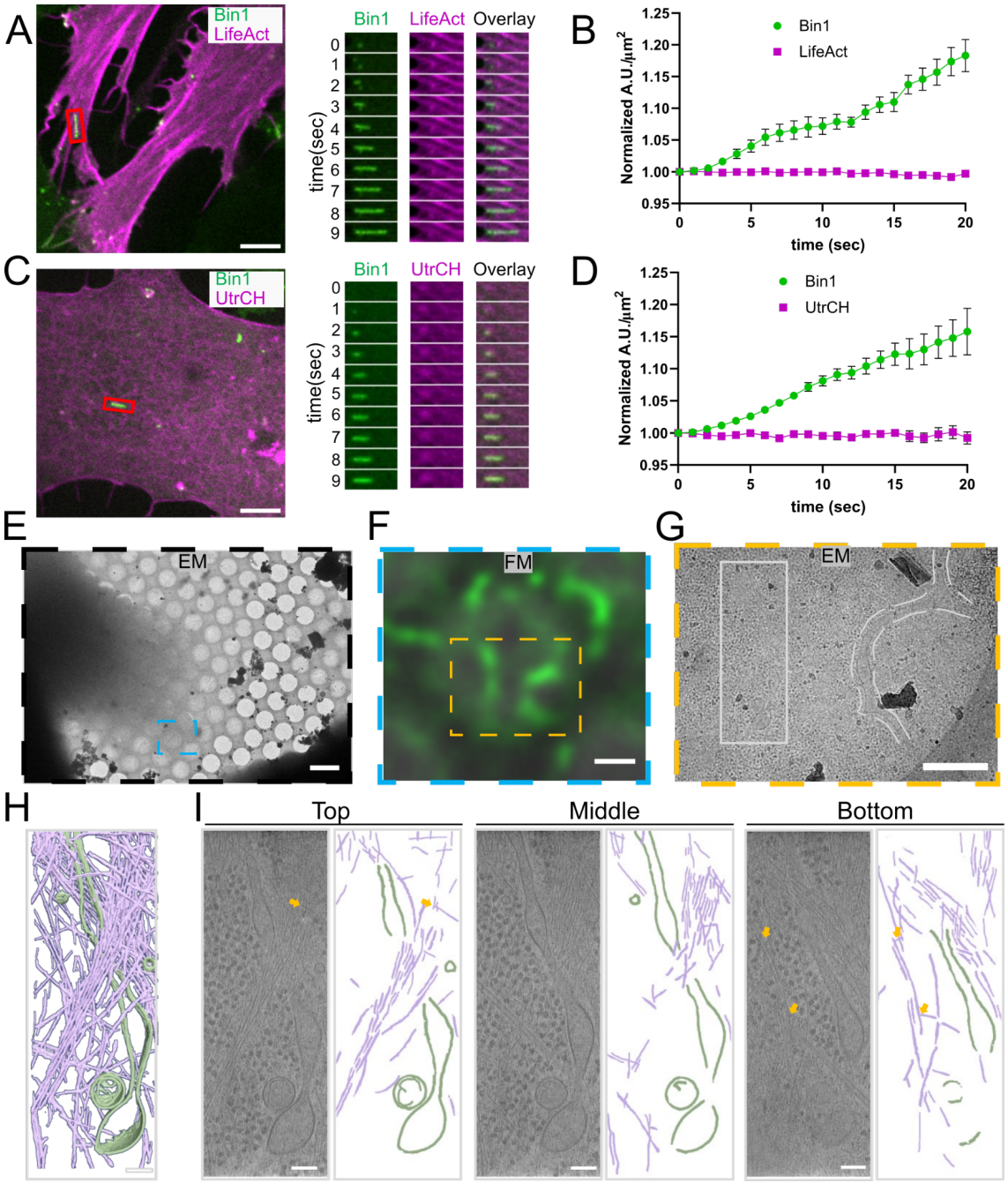

Fig. S2 – F-actin is not locally nucleated at growing tubules. **(A)** Left image corresponds to a timelapse snapshot of GFP-Bin1 myoblasts (green) and LifeAct-mCherry (magenta). Right image corresponds to kymographs from the red rectangle ROI showing a Bin1-tubule growing over time in the absence of F-actin changes. (**B**) Plots of LifeAct-mCherry and GFP-Bin1 average fluorescence intensity over time. Mean and SEM are represented. N=19 from two independent experiments. (**C**) Left image corresponds to a timelapse snapshot of GFP-Bin1 myoblasts (green) and mScarlet-I-UtrCH (magenta). Right image corresponds to kymographs from the red rectangle ROI showing a tubule growing over time in the absence of F-actin changes. (**D**) Plots of the mScarlet-I-UtrCH and GFP-Bin1 average fluorescence intensity over time. Mean and SEM are represented. N=16 from two independent experiments. (**E**) Representative low magnification cryo-EM image showing part of one cell on a TEM grid. The cyan rectangle indicates the ROI imaged using epifluorescence and brightfield microscopy (panel F). (**F**) Merged epifluorescence (green) and brightfield (grey, FM) image of the ROI. in E, showing multiple GFP-Bin1 tubules at the cell periphery. The orange rectangle indicates the ROI imaged using TEM (panel G). (**G**) Medium magnification TEM image of the ROI in F, showing the tubules observed in F. (**H**) 3D representation of cropped tomogram segmentation of the white rectangle ROI from G, with actin

filaments (purple) and tubule membrane (green). (**I**) Slices of the tomogram in H at different z positions (from left to right: z=-25nm, 30nm and 135nm relative to the central slice) with actin filaments (purple), tubule membrane (green), and potential actin branches (yellow arrows). Scale bar: 5 µm in A, C and E, 1 µm in F, 500 nm in G and 100 nm in H and I.

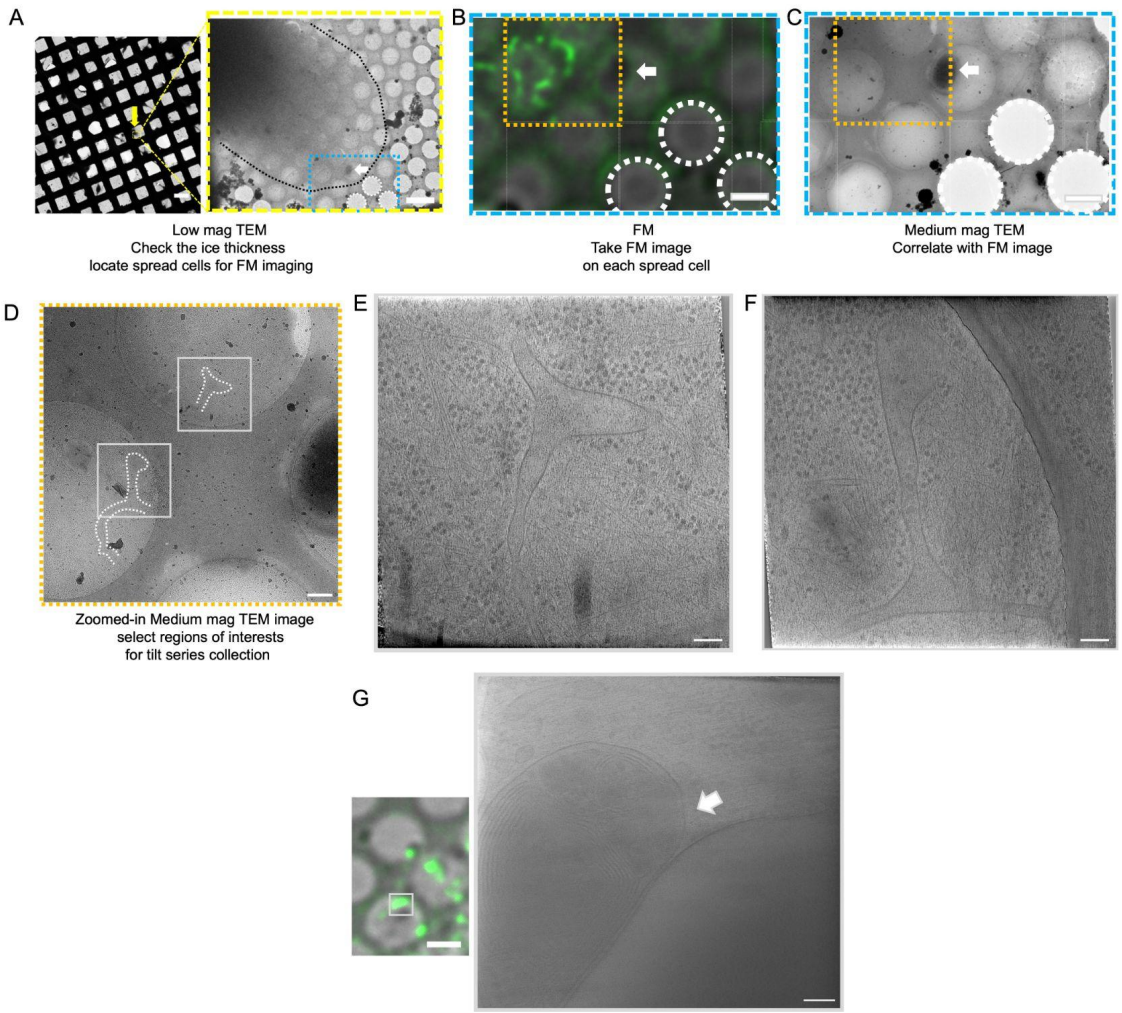

Fig. S3 - Correlative light and electron microscopy workflow.
(**A**) Cells were imaged using TEM to check the ice thickness and locate spread cells for FM imaging. In the example image, one spread cell is indicated with a yellow arrow, with the approximate cell periphery outlined in black in the zoomed view. (**B**) Cells imaged using cryo-fluorescence microscopy (FM) with the bright-field image of the area in the blue box from A showing the GFP-Bin1-labeled membrane tubule structures at the cell periphery. (**C**) Cells were re-imaged using medium magnification TEM images in tiles and combined for FM-TEM correlation. The empty holes and black features were used for manual correlation, with empty holes indicated by white circles and the dark feature marked by a white arrow. (**D**) A zoomed-in view of the medium magnification image collected from the orange region in C. Tubular membrane structures are highlighted with white curvy lines. The shapes of these tubular membrane structures resemble those seen in the FM image in B. Regions of interest (ROI) were selected for tilt series data collection, indicated by white boxes. (**E**) and (**F**) The central slice along the z-axis of the 3D tomogram at positions 1 and 2, respectively. (**G**) The bright-field and FM image showing fluorescently-labelled vesicular structure. A tomographic slice of the reconstruction inside the white box showing nested sets of membranes is shown on the right. Scale bar: 100 µm and 5 µm in A, 2 µm in B and C,500 nm in D, 100 nm in E and F. 2 µm and 100 nm in G.

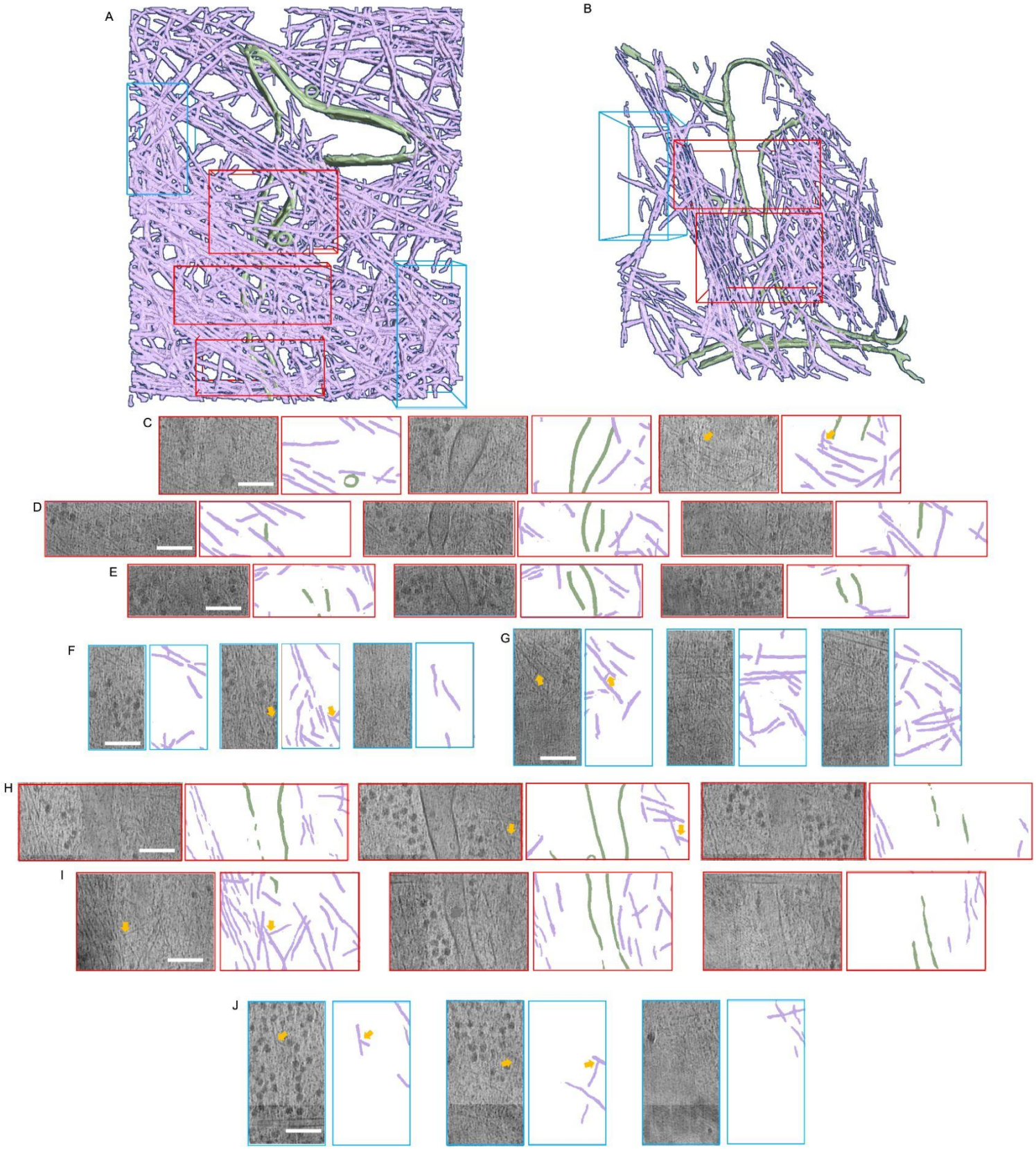

Fig. S4 - Quantitative analysis of cryo-electron tomograms. (**A**) 3D representation of cropped tomogram segmentation in fig S2E, sub-volumes proximal (red ROI) or distant (blue ROI) from tubule membrane used for counting branch number indicated with red boxes and blue boxes, respectively. (**B**) 3D representation of cropped tomogram segmentation in fig. S2F, sub-volumes

proximal to and distant from tubule membrane used for counting branch number indicated with red boxes and blue boxes, respectively. (**C**) Slices and segmentations of the tomogram in A in red box1 at different z positions (from left to right: z=-35nm, 5nm and 34nm relative to the central slice) with actin filaments in purple, tubules in green, and potential actin branches indicated with yellow arrows. Scale bar: 100 nm. (**D**) Slices and segmentations of the tomogram in A in red box2 at different z positions (from left to right: z=-26nm, 3nm and 28nm relative to the central slice) with actin filaments in purple, tubules in green.Scale bar: 100 nm. (**E**) Slices and segmentations of the tomogram in A in red box3 at different z positions (from left to right: z=1 nm, 14 nm and 34nm relative to the central slice) with actin filaments in purple, Tubules in green.Scale bar: 100 nm. (**F**) Slices and segmentations of the tomogram in in A blue box1 at different z positions (from left to right: z=-27 nm, 3 nm and 22 nm relative to the central slice) with actin filaments in purple, tubules in green, and potential actin branches indicated with yellow arrows. Scale bar: 100 nm. (**G**) Slices and segmentations of the tomogram in A in blue box2 at different z positions (from left to right: z=-13nm, 10nm and 31nm relative to the central slice) with actin filaments in purple, tubules in green, and potential actin branches indicated with yellow arrows. Scale bar: 100 nm. (**H**) Slices and segmentations of the tomogram in B in red box1 at different z positions (from left to right: z=-15nm, 11nm and 34nm relative to the central slice) with actin filaments in purple, tubules in green, and potential actin branches indicated with yellow arrows. Scale bar: 100 nm. (**I**) Slices and segmentations of the tomogram in B in red box2 at different z positions (from left to right: z=-22 nm, 7 nm and 30 nm relative to the central slice) with actin filaments in purple, tubules in green, and potential actin branches indicated with yellow arrows. Scale bar: 100 nm. (**J**) Slices and segmentations of the tomogram in B in blue box at different z positions (from left to right: z=-14 nm, 16 nm and 39 nm relative to the central slice) with actin filaments in purple, tubules in green, and potential actin branches indicated with yellow arrows. Scale bar: 100 nm.

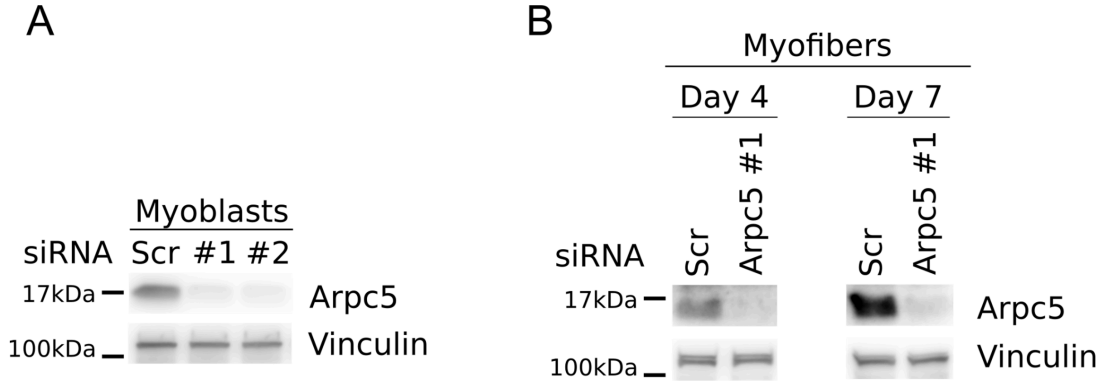

Fig. S5 - Western blots of Arpc5 depletion. (**A**) Western blots of GFP-Bin1 myoblasts knocked down for scramble (Scr), Arpc5 #1 (ID#s85623) or Arpc5#2 (ID#s85621). Membranes were blotted using antibodies against Arpc5 with vinculin as a loading control. (**B**) Western blots of myofibers (differentiation day 4 or 7), knocked down for scramble (Scr) or Arpc5 #1. Membranes were blotted using antibodies against Arpc5 and vinculin, used as a loading control.

Movies

Movie S1 – Timelapse movie of t-tubule dynamics in a myofiber isolated from the EDL muscle of an adult mouse. Isolated fiber was stained with CellMask to label t-tubules. Scale bar 5 µm.
Movie S2 – Timelapse movie of t-tubule dynamics in a developing in vitro myofiber. Cells were stained with CellMask to label t-tubules. Scale bar 5 µm.
Movie S3 – Timelapse movie of Triadin (green) and t-tubule (magenta) dynamics in a developing in vitro myofiber. Cells expressing Triadin-GFP stained with CellMask to label t-tubules. Scale bar 5 µm.
Movie S4 – Timelapse movie of t-tubule dynamics in a developing myofiber before (left panel) or 5 min after (right panel) adding CK666. Cells were stained with CellMask to label t-tubules. Scale bar 5 µm.
Movie S5 – Timelapse movie of tubule dynamics in GFP-Bin1 myoblasts before and after adding CK666. Scale bar 5 µm.
Movie S6 – F-actin (LifeAct-mCherry, magenta) and Bin1 tubules (GFP-Bin1, green) in GFP-Bin1 myoblasts. Scale bar 5 µm.
Movie S7 – F-actin (mScarlet-i-UtrCH, magenta) and Bin1 tubules (GFP-Bin1, green) in GFP-Bin1 myoblasts. Scale bar 5 µm.
Movie S8 – Cryo-electron tomogram and segmentation model of actin cytoskeleton around t-tubule site. Actin cytoskeleton coloured in light purple. T-tubule membrane coloured in green.
Movie S9 – Cryo-electron tomogram and segmentation model of actin cytoskeleton around t-tubule site. Actin cytoskeleton coloured in light purple. T-tubule membrane coloured in green.
Movie S10 – Cryo-electron tomogram and segmentation model of actin cytoskeleton around t-tubule site. Actin cytoskeleton coloured in light purple. T-tubule membrane coloured in green.
Movie S11 – Timelapse movie of tubule dynamics in GFP-Bin1 myoblasts before and after adding para-aminoblebbistatin (+Blebb). Scale Bar 5 µm.
Movie S12 – Timelapse movie of t-tubule dynamics in a developing in vitro myofiber before (left panel) or 5 min after (right panel) adding para-aminoblebbistatin (+Blebb). Cells were stained with CellMask to label t-tubules. Scale bar 5 µm.
Movie S13 - Timelapse movie of tubule dynamics in GFP-Bin1 myoblasts before and after adding glycerol. Scale Bar 5 µm.
Movie S14 - Timelapse movie of t-tubule dynamics in a developing myofiber before (left panel) or after (right panel) adding glycerol. Cells were stained with CellMask to label t-tubules. Scale bar 5 µm.
Movie S15 - Timelapse movie of tubule dynamics in GFP-Bin1 myoblasts before and after adding NSC668394 (+NSC). Scale Bar 5 µm.
Movie S16 – Timelapse movie of t-tubule dynamics in a developing in vitro myofiber before (left panel) or 5 min after (right panel) adding NSC668394 (+NSC). Cells were stained with CellMask to label t-tubules. Scale bar 5 µm.
Movie S17 – Timelapse movie of tubule dynamics in GFP-Bin1 myoblasts depleted for scramble control (left panel) or depleted for Arpc5 siRNA#1. Scale bar 5 µm.
Movie S18 – Timelapse movie of t-tubule dynamics in a developing myofiber in scramble cells (top panel) or in cells depleted for Arpc5 (bottom panel). T-tubules were stained with CellMask. Scale bar 5 µm.